Exposure assessment in near-field : methodology and application in FM frequencies for occupational exposure

Bader Mustafa Fetouri

INSTITUT POLYTECHNIQUE DE PARIS

NNT : 2021IPPAT020

Thèse de doctorat

Exposure Assessment in Near-field: New Methodology and Application in FM Frequencies for Occupational Exposure

Thèse de doctorat de l'Institut Polytechnique de Paris
préparée à Télécom Paris

École doctorale n°626 École doctorale de l'Institut Polytechnique de Paris (EDIPP)
Spécialité de doctorat : Physique

Thèse présentée et soutenue à Palaiseau, le 18 Juin 2021, par

BADER FETOURI

Composition du Jury :

Christian Person IMT Atlantique	Président et Rapporteur
David Lautru Université Paris Nanterre	Rapporteur
Shermila Mostarshedi Université Gustave Eiffel	Examinatrice
Christophe Roblin Ecole Télécom Paris	Examinateur
Joe Wiart Ecole Télécom Paris	Directeur de thèse
Philippe De Doncker Université Libre de Bruxelles	Co-directeur de thèse
Allal Ouberehil TDF Rennes	Invité

Acknowledgements

The hour of work has struck,
and so let us forge ahead.

Salem Abu-Minyar

First and foremost, I would like to praise *God, the Almighty,* who has granted me countless blessings, knowledge, and opportunity, so that I have been finally able to complete the thesis. Secondly, this work would not have been possible without the dedication and guidance of people to whom I am grateful.

I would like to thank my Ph.D. thesis referees Dr. Christian Person and Dr. David Lautru for reviewing my manuscript. I would like to thank Dr. David Lautru, Dr. Shermila Mostarshedi, and Dr. Christophe Roblin for being part of the thesis evaluation committee.

I would like to thank the TDF team, especially Mr. Allal Ouberehil and Mr. Philippe Briend for their support, industry insights, and discussions throughout my Ph.D.

I would like to express my sincere gratitude to my supervisors Dr. Joe Wiart and Dr. Philippe De Doncker for the continuous support of my research during my Ph.D., for their patience, and their shared knowledge. Their guidance helped me throughout the research and writing of this thesis.

I thank my colleagues Amirreza, Maruf, Soumaya, Yuanyuan, Seyedfaraz, Ziecheng, Xi, Taghrid, Shanshan, and Mauricio for the interesting discussions and for the fun times we have shared.

I am tremendously grateful to my parents, my wife, my brother, my sister, my cousins, and my friends for their support and help.

Abstract

FM radio is still popular among all segments of the general population. FM antenna arrays are usually placed on metallic structures known as pylons that workers have to climb in order to do maintenance and repair work. Exposure monitoring is required by regulation when workers are exposed to high-power emitters. The purpose of this research is to characterize electromagnetic fields (EMF) in pylon environments and to assess EMF exposure in such cases.

EMF in pylon environments tend to be in the near-field region of the antenna arrays, but the characterization and understanding of such environments in the literature is limited to specific exposure cases. This research has therefore focused on defining a new methodology by generalizing exposure assessment in the near-field.

Using field metrics analysis in human-sized volumes, this study analyzed the near-field environments found in the transmission pylons and generated random incident fields that have the same characteristics. The random incident fields were subjected to a validation and selection process in order to be used in FDTD simulations for specific absorption rate (SAR) assessment.

Five hundred FDTD simulations for SAR assessments were performed. The results showed a high correlation between local & whole-body SAR and averaged electric field strength. Surrogate models linking SAR to electric field strength were built using machine learning techniques. The uncertainty of the SAR results and the surrogate models was quantified.

Résumé

La radio FM reste populaire chez toutes les catégories du grand public. Ainsi, les antennes FM sont généralement placées sur des structures métalliques, aussi appelées pylônes, que les travailleurs doivent escalader pour effectuer des travaux de maintenance. La législation exige le contrôle de l'exposition lorsque les travailleurs sont exposés à des émetteurs à haute puissance. L'exposition est évaluée en termes de restrictions de base et de niveaux de références. Les restrictions de base nécessitent de déterminer le DAS (débit d'absorption spécifique), c'est-à-dire la puissance absorbée par un individu via l'émission d'ondes électromagnétiques. L'évaluation du DAS nécessitant des mesures invasives, il a été défini des niveaux de références permettant d'avoir des gabarits exprimés en termes de valeur de champ électrique et/ou magnétique et/ou de densité de puissance en fonction de la fréquence de la source d'émission.

Les champs électromagnétiques dans les environnements des pylônes sont généralement dans le champ proche des antennes, mais la caractérisation et la compréhension du champ proche dans la littérature est limitée à des cas spécifiques d'exposition, qui ne représentent pas la haute variabilité des champs électromagnétiques en champ proche dans les pylônes. L'objectif de cette thèse est de déterminer une nouvelle méthodologie pour définir des niveaux de références pour les travailleurs en zone de champ proche appliquée dans l'environnement des pylônes de la radiodiffusion FM. Une partie du travail a consisté à rappeler les différentes règles pour distinguer la zone de champ lointain, de la zone de champ proche d'une antenne d'émission, ainsi que celle qui sera prise par la suite dans l'étude.

La méthodologie employée pour évaluer l'exposition en champ proche se décompose en deux étapes majeures, la génération de champ puis le calcul des niveaux d'expositions. Afin d'être décorrélé des niveaux de DAS par rapport aux situations d'expositions, problème inhérent à la dosimétrie en champ proche, ce travail propose de générer des champs électromagnétiques aléatoires. Ces derniers sont sélectionnés afin d'avoir des caractéristiques similaires à ceux que l'on peut trouver à l'intérieur des pylônes de la radiodiffusion FM. Ce générateur de champs aléatoire, spécifique de ce que l'on peut trouver à l'intérieur des pylônes, servira d'entrée à un simulateur électromagnétique, basé sur la méthode des différences finies dans le domaine

temporel (FDTD), pour calculer DAS local et corps entier pour n'importe quelle situation d'exposition.

Afin de pouvoir comparer le champ généré aléatoirement avec celui qui se trouve à l'intérieur des pylônes quatre indicateurs ont été définis. Deux sont corrélés avec la notion de champ proche et les deux autres au DAS. Ainsi une métrique est définie pour faciliter la comparaison du champ électromagnétique produit à l'intérieur de soixante-quatre configurations de pylônes, déterminé par un simulateur électromagnétique commercial et qui constitue une base de référence, avec celui du générateur de champ proche aléatoire.

Afin de valider le fonctionnement de la méthodologie proposée, une comparaison d'histogrammes est réalisée entre les quatre indicateurs produits par le générateur aléatoire de champ proche et ceux de la base de référence. Trois tests statistiques différents sont réalisés pour évaluer la ressemble entre les histogrammes. Puis la sélection des 500 expositions de champs électromagnétiques pour le calcul de DAS produit par le générateur aléatoire de champ proche, en accord avec la base de référence, sont réalisés en effectuant un tirage suivant une loi uniforme. Pour le calcul du DAS, une méthode d'homogénéisation est utilisée pour réduire d'un facteur 16 le temps de calcul d'une simulation (12h), en acceptant d'avoir une erreur de 8% sur l'amplitude du champ électrique, répercutant une erreur de 16% sur le DAS, à la fréquence de 100 MHz.

Les résultats de simulations FDTD montrent une forte corrélation entre le DAS local/corps entiers et le champ électrique moyen. En partant de l'hypothèse que le DAS du corps entier est corrélé avec l'amplitude moyenne du champ électrique élevé au carré, un modèle de régression linéaire est proposé. Aussi, un travail analogue est réalisé avec le DAS local, en partant de l'hypothèse qu'il est corrélé avec l'amplitude moyenne du champ électrique élevée au carré et avec l'amplitude maximum du champ électrique élevée au carré. L'étude a été menée pour une fréquence fixe de 100 MHz mais qui peut s'étendre à la bande de fréquence commerciale FM de 87,5 MHz à 108 MHz moyennant une erreur maximale de 5%.

Contents

List of Figures

List of Tables

Chapter 1

Introduction

1.1 General motivations

The increasing use of wireless communication has strengthened the need for exposure monitoring, in particular near antennas where workers are likely to be exposed. The International Commission on Non-Ionizing Radiation Protection (ICNIRP) [ICN20] and the IEEE-International Committee on Electromagnetic Society (IEEE-ICES) [IEE19] have recommended protection limits for EMF exposure. These limits, composed of basic restrictions and reference levels, are set to avoid any health effects due to EMF exposure. Basic restrictions are the fundamental exposure limits and were established to limit in the RF domain the specific absorption rate (SAR) that represents the absorbed power per unit mass of tissue in the human body. The basic restrictions define the whole-body SAR as well as the local SAR limits that quantify the SAR averaged over 10 grams of tissue. Basic restrictions assessment is almost impossible in-situ since they are too complex to measure and are generally computed. Therefore derived limits were defined, known as reference levels in terms of electric and magnetic field strength. The compliance to RLs ensures compliance to basic restrictions. Reference levels are conservative and are often used because of their convenience. In Europe, the directive 2013/35/EU [Eur13], partly based on ICNIRP [Gui98] and IEEE-ICES [IEE10], requests to monitor the workers' exposure to electromagnetic fields (EMF) to prevent any overexposure. Reference levels are used as action values in the European directive 2013/35/EU.

1.2 Thesis context and motivations

FM transmitters used in broadcasting are located on towers that workers have to climb in order to do maintenance and repair work. Occupational exposure to electromagnetic fields must be monitored in these situations. Fields emitted by FM transmitters inside the pylons where workers intervene are difficult to assess because they are in the near-field region of the FM antennas. Since SAR cannot be measured on site, broadcasting operators use field meters to ensure their workers are not exposed to field levels above reference levels. The aim of the study is to analyze the behavior of the field nearby the FM antennas and to establish a relationship between the basic restrictions and the electric field strength in these environments.

ICNIRP guidelines and IEEE-ICES 2019 standard provide reference levels for far-field and near-field exposure cases. The estimation of the exposure far from transmitters known as far-field exposure is well-referenced and its on-site practices are known. However, the near-field reference levels given by ICNIRP guidelines [ICN20] and IEEE-ICES 2019 [IEE19] standard are based on a near-field definition that is questioned in this study. This work proposes a method that can generalize the near-field human exposure assessment, taking into account the near-field characteristics of the electromagnetic field. In order to study broadly the near-field exposure, near-fields with adjustable characteristics were generated. The local & whole-body SAR results were studied. Estimation formulas to find basic restrictions from reference levels in pylon environments are proposed. Such a relationship will facilitate the estimation of SAR in real-time in FM near-field exposure.

1.3 Organization of the dissertation

This PhD thesis is divided into 5 chapters.

In chapter 2, a literature review of near-field exposure assessment is presented, which includes used standards and regulation, near-field definitions, and exposure assessment studies performed in the near-field.

The near-field exposure assessment methodology is presented in chapter 3. The methodology includes pylons simulations for reference, random near-field generation, and the near-field characterization method.

Chapter 4 proposed a validation of the near-field exposure assessment methodology presented in chapter 3, as well as the human exposure computation material required for SAR simulations. A design of experiments for conducted SAR simulations is given.

Chapter 5 shows the results of SAR simulations and the surrogate models which link basic restrictions to reference levels.

Chapter 6 concludes the PhD thesis.

Chapter 2

Occupational RF Exposure and near-field exposure assessment

2.1 Human exposure in standards and regulation framework

2.1.1 Exposure metrics

Absorption and SAR

The electromagnetic fields (EMF) induced by a source are composed of electric and magnetic field that are governed by Maxwell's equations. The human exposure to EMF sources is quantified using the specific absorption rate (SAR) that is the absorbed power by the human body when exposed to EMF. SAR is defined as the absorbed power from EMF by the human body tissues divided by the mass of said tissues in kilograms:

$$SAR = \frac{Absorbed\ power\ in\ \mathrm{W}}{Mass\ in\ \mathrm{kg}} \tag{2.1}$$

SAR can be quantified over the entire body or over a specific organ in the human body. Existing standards (ICNIRP and IEEE-ICES, see 2.1.2) in EMF exposure define the whole-body SAR (WBSAR) by summing the absorbed energy of each tissue, and the local SAR as the SAR measured over 1 or 10 grams of tissue. SAR is usually assessed using the electric field found in a tissue. Equation 2.2 explains the relationship between SAR and electric field.

$$SAR = \frac{\sigma E^2}{2\rho} \tag{2.2}$$

E is the electric field in V/m, ρ is the tissue density in kg/m^3, and σ is the electric conductivity of the tissue in S/m.

Protection Limits

The International Commission on Non-Ionizing Radiation Protection (ICNIRP) [ICN20] and the IEEE-International Committee on Electromagnetic Society (IEEE-ICES) [IEE19] have recommended protection limits for EMF exposure. These limits are composed of basic restrictions and reference levels and are set to avoid any health effect to acute exposure due temperature rise in the human body. Basic restrictions are the fundamental exposure limits and were established to limit in the radiofrequency (RF) domain the SAR. The basic restrictions define the whole-body SAR as well as the local SAR

limits that quantify the maximum SAR averaged over 10 grams of tissue. Basic restrictions assessment is almost impossible in-situ since they are too complex to measure and are generally computed. Therefore derived limits were defined, known as reference levels in terms of electric and magnetic field strength, or power density. The compliance to reference levels insures compliance to basic restrictions. Reference levels were defined first for whole-body SAR in [Gui98] and in [IEE10], but then reference levels for local SAR were given in [ICN20] and in [IEE19] at later dates. Reference levels are conservative and are often used because of their convenience, as they only require the use of a field meter on site.

SAR assessment using numerical methods

Numerical assessment of SAR requires the modeling of the sources, the human body, and the environment. Sources emit electromagnetic fields that can be found using various numerical techniques, such as the well-known Finite Difference in Time Domain (FDTD),Finite Integration Technique, or the Method of Moments, and the use of mathematical routines to decompose any field using the Plane Wave expansion method [Goo05] or the Spherical Waves expansion method [HJ88].

The human body was modeled using Magnetic Resonance Imaging (MRI) by representing the body as a series of voxel images of thin slices. Each voxel corresponds to a type of body tissue (fat, muscle, blood, etc.) with its own dielectric properties (namely permittivity in F/m, permeability in H/m, density in kg/m^3, and tissue conductivity in S/m). Among many works that have modeled the human body, the Foundation for Research on Information Technology in Society (IT'IS) has presented human models for adults and children [CKH$^+$09], as shown on figure 2.1. The dielectric properties of the tissues in the human models are measured and used to assess SAR using equations 2.1 and 2.2. Tissues conductivities can be assigned using the IT'IS database [HNG$^+$12] or the FCC database [C$^+$18]. An example of the dielectric properties on the Duke human model can be seen on figure 2.2.

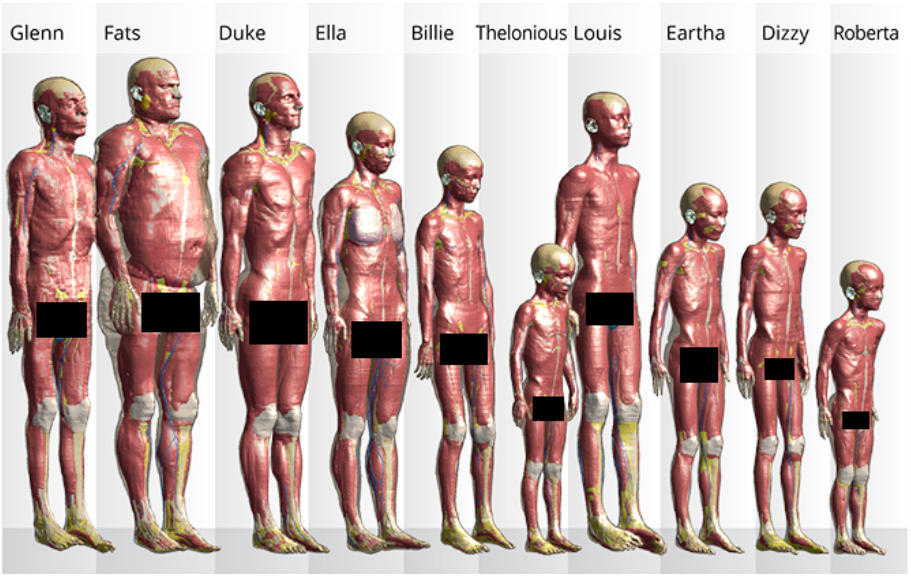

Figure 2.1: Human models of adults and children.

Age	34 years
Height	1,77 m
Weight	70,2 kg
Number of tissues	47

Tissue	Conductivity σ ($f = 100\ MHz$)	Density ρ
Air (vacuum)	0	0
Blood	1,23	1060
Veins	0,46	1060
Spinal fluid	0,02	1038
Skin	0,49	1100

$$SAR = \frac{\sigma E^2}{2\rho}$$

Figure 2.2: Duke human model description and dielectric properties.

SAR transfer functions

SAR assessment using measurements is complex and time-consuming. Multiple studies were conducted to find transfer functions to make SAR assessment possible by using the electric field or power density. One study [GVK+11] looked at estimation formulas in case of an exposure to base-station antennas, for frequencies from 300 MHz to 5 GHz. The study exposed male and female adults, and children to generic base-station antennas radiation using a 95-th cuboid method, which allows to find conservative SAR estimation formulas for 95% of the population. The estimation formulas are not applicable in the reactive near-field, because of the field variability in that field region, explained in section 2.2.1.

Reference [CHL+08] looked at child and adult models exposed to plane waves for frequencies from 20 MHz to 2.4 GHz. Whole-body averaged SAR values were given in each case, with the average SAR value per specific body tissue (skin, fat, muscle, etc.). The study showed a "resonance" frequency range from 40 to 80 MHz, in which the human body absorbed more power. This is due to wavelength being closer to the human body size, which causes the human body to act as a passive antenna. The resonance phenomenon of the human body can be seen on figure 2.3.

In another study [KCH+11a], the values of whole-body SAR are computed at 2.1 GHz for a V-polarized plane wave and for azimuth incident angles varying between 0 deg and 360 deg. Whole-body SAR is shown to vary depending on the angle of the incident plane wave (figure 2.4). Whole-body SAR is maximal when the plane wave is facing the front of the human model. According to [CHG+10], horizontal plane waves induce a whole-body SAR up to 30 % higher than the vertical plane waves. In addition to the incident angle of a plane wave, body posture is shown to have an impact on whole-body SAR [FD05] (see figure 2.5).

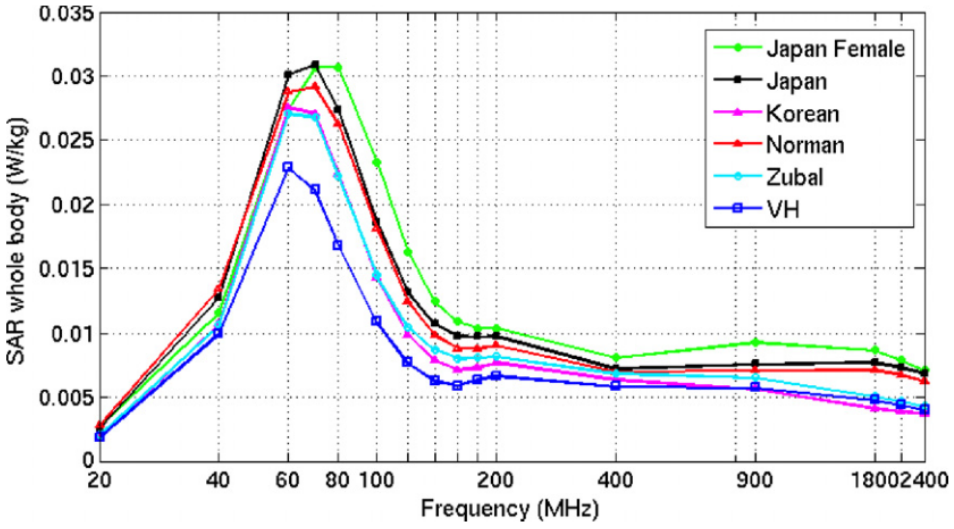

Figure 2.3: Whole-body-averaged SAR for different adult models on a large frequency range from 20 MHz to 2400 MHz for an incident power density of 1 W/m^2 [CHL$^+$08].

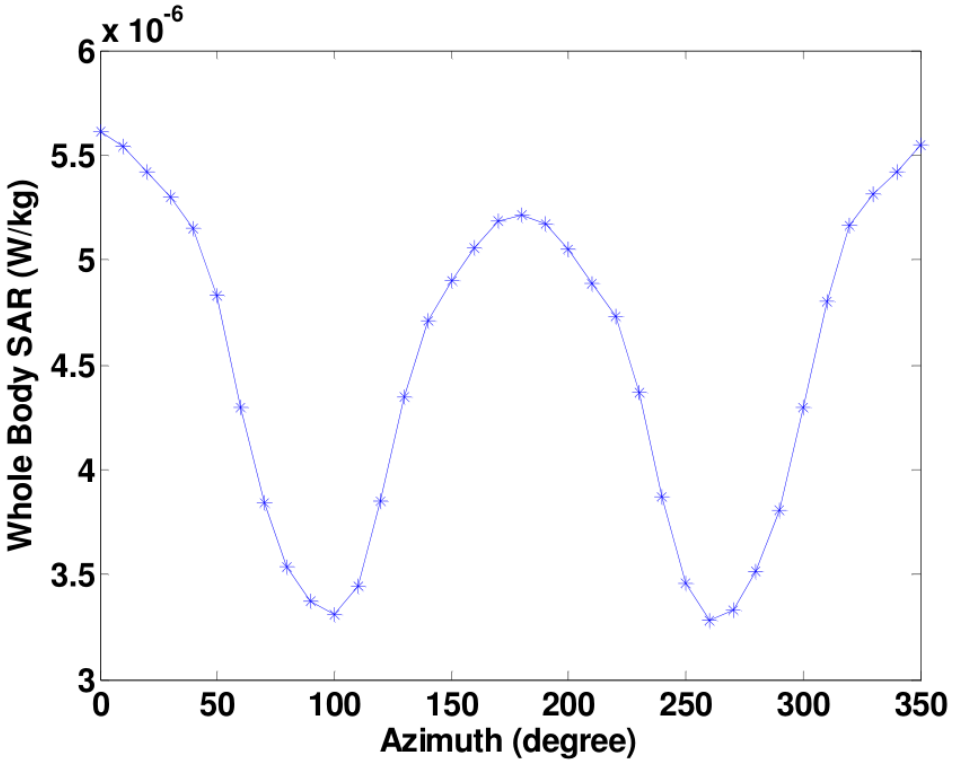

Figure 2.4: Whole-body averaged SAR for an incident single plane wave and a 10 deg azimuth angle step [KCH+11a].

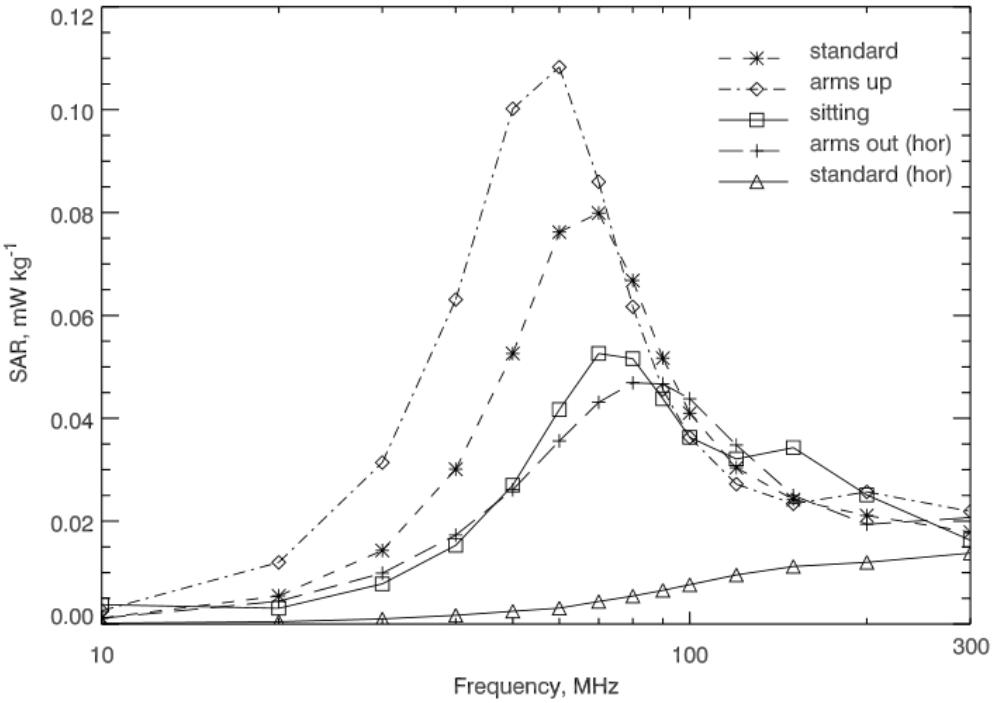

Figure 2.5: Whole-body averaged SAR for different body postures. Incident electric field is 1 V/m [FD05].

2.1.2 Standards: ICNIRP and IEEE-ICES

Dosimetric Reference Levels: Basic Restrictions

According to [ICN20] and [IEE19], whole-body SAR is to be averaged over 30 minutes whereas local SAR exposure is to be averaged over 6 minutes. Whole-body and local SAR levels must be compliant with basic restrictions indicated in table 2.1. Both standards divide basic restrictions levels into two groups: general public and workers. General public (also known as persons in unrestricted environments in [IEE19]) designates general people of all ages and genders, and are assumed to be in untrained in the matters of EMF exposure. Workers (also known as persons permitted in restricted environments) are people who are aware of their exposure to EMF and have been trained on what precautions must be taken around active emitters. Local exposure levels differ depending on the position on the human body, since head and torso are believed to be more sensitive to health effects caused by EMF exposure than limbs and pinnae.

Conditions	General Public SAR (W/kg)	Workers SAR (W/kg)
Whole-body exposure	0.08	0.4
Local exposure (head and torso)	2	10
Local exposure (limbs and pinnae)	4	20

Table 2.1: Basic restrictions for electromagnetic field exposure from 100 kHz to 6 GHz, according to [ICN20] and [IEE19].

Exposure Reference Levels: Maximum Field Strength

Exposure reference levels were derived from basic restrictions to facilitate SAR assessment in any given environment, by providing measurable electric and magnetic field values that can be found on-site by using a fieldmeter. Reference levels are therefore expressed as electric fields in V/m, magnetic fields in A/m or power density $\mathbf{S}$ in W/m^2, which is defined as the real part of the complex Poynting vector: $\mathbf{S} = \frac{1}{2}\Re(\mathbf{E} \times \mathbf{H}^*)$. ICNIRP guidelines 2020

[ICN20] and IEEE 2019 [IEE19] indicate reference levels for both whole-body and local exposure. In the beginning of the PhD work presented in this document, reference levels for local exposure did not exist, as older issues of ICNIRP ([Gui98]) and IEEE ([IEE10]) only provided reference levels for whole-body exposure. The equivalent surface of a wavelength varies as the frequency changes, therefore reference levels are frequency-dependent, unlike basic restrictions. References levels as indicated in ICNIRP 2020 guidelines are shown on tables 2.2 and 2.3.

Exposure scenario	Frequency range	E-field strength E (V/m)	H-field strength H (A/m)	Incident power S (W/m^2)
Occupational	$0.1 - 30$ MHz	$660/f^{0.7}$	$4.9/f$	NA
	$> 30 - 400$ MHz	61	0.16	10
	$> 400 - 2000$ MHz	$3f^{0.5}$	$0.008f^{0.5}$	$f/40$
	$> 2 - 6$ GHz	NA	NA	50
General public	$0.1 - 30$ MHz	$300/f^{0.7}$	$2.2/f$	NA
	$> 30 - 400$ MHz	27.7	0.073	2
	$> 400 - 2000$ MHz	$1.375/f^{0.5}$	$0.0037/f^{0.5}$	$f/200$
	$> 2 - 6$ GHz	NA	NA	10

1. "NA" mean "not applicable" and should not be taken into account.
2. f is the frequency in MHz.
3. S, E and H are to be averaged over 30 minutes, over the whole-body space.
4. For $0.1 \geq f > 30$ MHz, compliance is demonstrated if neither E or H exceeds the above reference level values.
5. For $30 > f > 2000$ MHz:
(a) in the far-field, compliance is demonstrated if either S, H or H does not exceed reference levels;
(b) in the radiative near-field zone, compliance is demonstrated if either S, or both E and H does not exceed reference levels;
(c) in the reactive near-field zone, compliance is demonstrated if both E and H do not exceed the reference levels, S cannot be used to demonstrate compliance, and so basic restrictions must be applied.

Table 2.2: Reference levels for whole-body exposure from 100 kHz to 6 GHz, averaged over 30 minutes and the whole body, unperturbed rms values, according to ICNIRP 2020 guidelines [ICN20].

Exposure scenario	Frequency range	E-field strength E (V/m)	H-field strength H (A/m)	Incident power S (W/m^2)
Occupational	$0.1 - 30$ MHz	$1504/f^{0.7}$	$10.8/f$	NA
	$> 30 - 400$ MHz	139	0.36	50
	$> 400 - 2000$ MHz	$10.58f^{0.5}$	$0.0274f^{0.5}$	$0.29f^{0.86}$
	$> 2 - 6$ GHz	NA	NA	200
General public	$0.1 - 30$ MHz	$671/f^{0.7}$	$4.9/f$	NA
	$> 30 - 400$ MHz	62	0.163	10
	$> 400 - 2000$ MHz	$4.72/f^{0.43}$	$0.0123/f^{0.43}$	$0.058f^{0.86}$
	$> 2 - 6$ GHz	NA	NA	40

1. "NA" means "not applicable" and should not be taken into account.
2. f is the frequency in MHz.
3. S, E and H are to be averaged over 6 minutes, over the relevant projected body space.
4. For $0.1 \geq f > 30\ MHz$, compliance is demonstrated if neither peak spatial E or peak spatial H exceeds the above reference level values.
5. For $30 > f > 6000$ MHz:
(a) in the far-field, compliance is demonstrated if either peak spatial S, E or H, over the projected whole-body space, does not exceed reference levels (only one is required);
(b) in the radiative near-field zone, compliance is demonstrated if either S, or both E and H, over the projected whole-body space, does not exceed reference levels;
(c) in the reactive near-field zone, compliance is demonstrated if both E and H do not exceed the reference levels, S cannot be used to demonstrate compliance, for $f > 2$ GHz reference levels cannot be used to determine compliance, and so basic restrictions must be applied.

Table 2.3: Reference levels for local exposure from 100 kHz to 6 GHz, averaged over 6 minutes locally, unperturbed rms values, according to ICNIRP 2020 guidelines [ICN20].

2.1.3 Regulation in Europe

Workers Directive 2013/35/EU

The European Parliament directive 2013/35/EU [Eur13] "lays down minimum requirements for the protection of workers from risks to their health and safety likely to arise from exposure to electromagnetic fields during their work". The directive defines basic restrictions as exposure limit values (ELVs) and reference levels as action levels (ALs). The directive requires the employer to assess the workers' exposure to EMF, by controlling ELVs and ALs. ELVs are the same as basic restrictions shown in table 2.1. ALs in terms of electric and magnetic field strengths are given for whole-body SAR but not for local SAR, as the directive 2013/35/EU is mainly based on [Gui98]. The directive specifies protection measures for workers, such as the training

of workers in regards to EMF exposure, the bonding of workers with work objects, the use of insulating shoes, gloves and protective clothing when applicable.

Radio Equipment Directive 2014/53/EU

The European Parliament directive 2014/53/EU [Eur14] establishes a "regulatory framework for the making available on the market and putting into service in the Union of radio equipment". The directive specifies radio equipment construction requirements such as the protection of health and safety of persons, domestic animals and private property, the electromagnetic compatibility of the equipment, the support and efficient use of radio spectrum to avoid harmful interference, the access to emergency services. The directive also specifies obligations on manufacturers, importers and distributors of radio equipment in the European Union.

2.2 Near-field exposure assessment state of the art

2.2.1 Near-field and exposure

Near-field definitions and characteristics

According to [Bal16], "the space surrounding an antenna is usually subdivided into three regions: reactive near-field, radiating near-field and far-field". Let R_1 and R_2 be the distances from the antenna to respectively the reactive near-field and radiating near-field. The well-known field regions formulas for distances R_1 and R_2 are defined as [Bal16]:

$$\begin{aligned} R_1 &= 0.62\sqrt{D^3/\lambda} \\ R_2 &= 2D^2/\lambda \end{aligned} \tag{2.3}$$

λ and D in equation 2.3 are respectively the wavelength and the largest dimension of the antenna, both in meters. In this situation, a distance $r < R_1$ is considered in the reactive near-field, whereas a distance $R_2 > r \geq R_1$ is considered in the radiative near-field. Field regions can be seen on figure 2.6.

Other studies have debated equations 2.3 to define the different field regions.

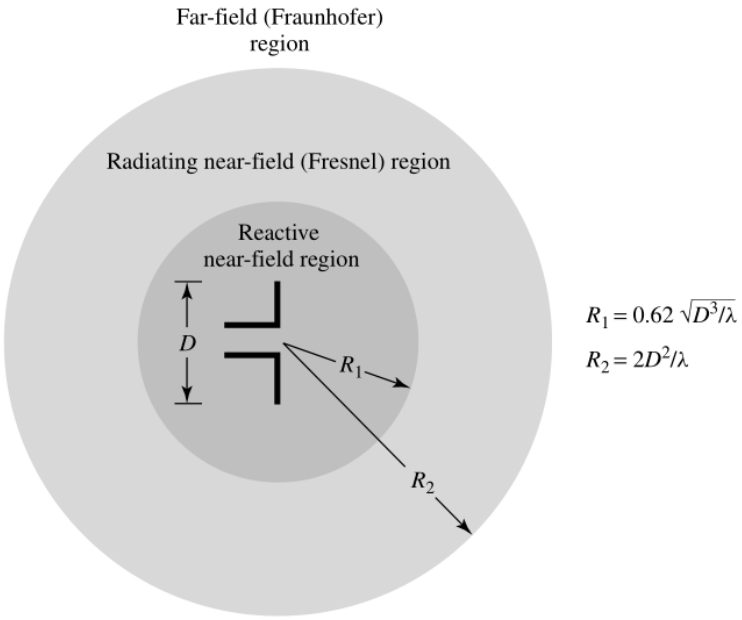

Figure 2.6: Field regions of an antenna [Bal16].

[Ban99] has found that supplementary conditions have to be respected in order to find the boundary between near-field and far-field. The widely known formula $r = 2D^2/\lambda$ to find the far-field is acceptable once equations 2.4 are verified.

$$\begin{aligned} r &> 2D^2/\lambda \\ r &> 5D \\ r &> 1.6\lambda \end{aligned} \tag{2.4}$$

In equations 2.4, r defines the distance between the antenna center and probe point.

Reference [LC04] has found other conditions to distinguish field regions. The study was performed on simple dipoles of multiple lengths and showed that the defining criteria for finding field regions are wave sphericity and field transversality. The criterion that shows the most restrictive field region boundary for a given dipole size defines the field distances for different

regions. For a $\lambda/2$ dipole, the different zones are defined as:

$$\begin{aligned} r_{VNF} &< 2\lambda \\ r_{FF} &< 9.5\lambda \end{aligned} \tag{2.5}$$

In equations 2.5, r_{VNF} is the very-near-field zone and r_{FF} is the far-field zone. For dipoles of different sizes, the near-field and far-field zones are defined differently [LC04]. [Bal16, Ban99, LC04] and equations 2.3 to 2.5 show that there are no reliable definitions of the different field regions. One must therefore find near-field characteristics that can at least reliably tell if the probe point is in the near-field or far-field.

Reference [VBPG15] indicates that the near-field characteristics can be identified through the wave impedance value and the angle formed between the electric field **E** and the magnetic field **H**. Based on reference [VBPG15], the wave impedance Z is defined in this work as the following:

$$\mathrm{Z} = \frac{|\mathbf{E}|}{|\mathbf{H}|} \tag{2.6}$$

The wave impedance and the angle formed between E and H are known to be constant in the far-field ($Z = Z_0 \approx 377\Omega$ and $(\widehat{\mathbf{E},\mathbf{H}}) = (\widehat{\mathbf{E},\mathbf{H}})_0 = \pi/2$, respectively), but not constant in the near-field and their values differs from Z_0 and $(\widehat{\mathbf{E},\mathbf{H}})_0 = \pi/2$, respectively [VBPG15]. The wave impedance and the angle between electric and magnetic field will therefore be used in this work to find out if a given distance is in the near-field.

To conclude, the near-field zone can be reliably identified through two different characteristics as shown in equations 2.7.

$$\begin{aligned} Z &\neq Z_0 \approx 377\ \Omega \\ (\widehat{\mathbf{E},\mathbf{H}}) &\neq \pi/2 \end{aligned} \tag{2.7}$$

Exposure assessment in the near-field according to ICNIRP and IEEE standards

According to both ICNIRP 2020 [ICN20] and IEEE 2019 [IEE19], a field region is considered in the far-field of an antenna when $r \geq 2D^2/\lambda$, where D and λ refer to the longest dimension of the antenna and wavelength, respectively, in meters. Both standards consider the distance from an antenna to

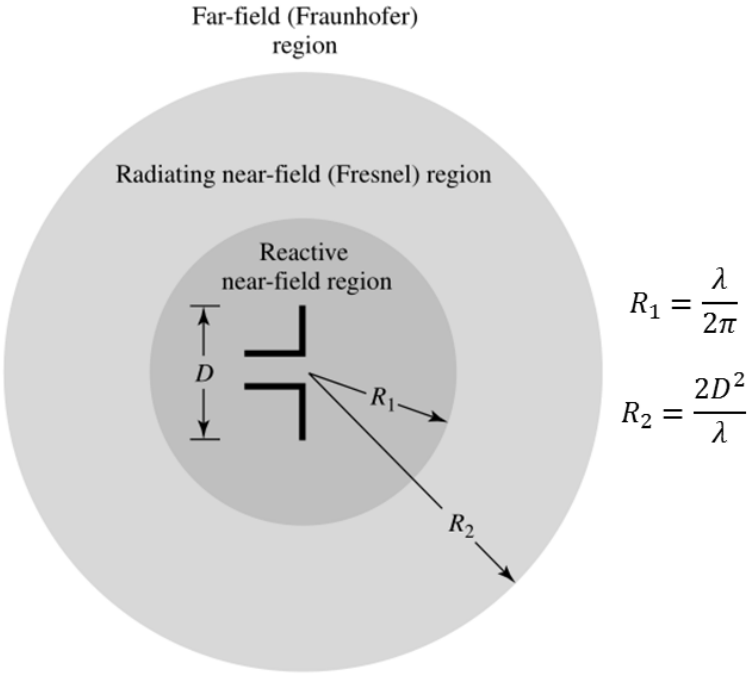

Figure 2.7: Field regions of an antenna, according to ICNIRP 2020 and IEEE 2019.

$\lambda/2\pi$ to be the reactive near-field, and the distance from $\lambda/2\pi$ to $2D^2/\lambda$ to be region where the field is the radiative near-field. Field regions according to standards can be seen on figure 2.7.

When it comes to exposure, both standards consider that reference levels can be exceeded if the basic restrictions are met. In the reactive near-field, both electric and magnetic field have to be assessed and cannot exceed reference levels. The power density cannot be used to assess reference levels in the reactive near-field. In the radiative near-field, either the power density S or both E and H can be used to assess exposure, and for compliance to be met, the reference levels cannot be exceeded. These distinctions are based on the fact that in the reactive near-field, E and H do not satisfy any wave impedance relation ($Z = \frac{E}{H}$ is not constant) have to be measured or computed separately [VBPG15]. In the radiative near-field, the wave impedance is considered to be almost constant [VBPG15], and so H can be approximated from

E.

Limits of usual near-field definitions for the exposure

The source dimension D in equations 2.3 is difficult to define in some situations. For example, in references [VKG12a, VKG12b], a human phantom is placed inside transmission pylons on which FM and DAB antennas are placed at different heights. In this context, the metallic structure of the transmission pylons itself can be considered as the source, since the radiation coming from the antennas will be diffracted by the metallic structure of the pylons. In such a situation, if one wants to find the near-field distance applicable to emitters, it is unclear if the antenna size D in equations 2.3 should the antenna dimension or the entire pylon's dimension which can be hundreds of meters.

The near-field definitions given in section 2.2.1 require the knowledge of the distance between the antenna and the probe point, and the largest dimension of the source causing the radiation. Both information can be difficult to find in certain exposure situations. Since multiple definitions were given for the near-field in section 2.2.1, none of them can be reliably used as they are debated. Furthermore, ICNIRP 2020 and IEEE 2019 define the reactive near-field region differently from equations 2.3. For all of these given reasons, we consider it is best to rely on near-field characteristics given by equations 2.7 to find whether an exposure assessment is happening in the near-field.

2.2.2 Limits of studies conducted with plane waves

Multiple studies were performed with plane waves in different conditions. They showed a plane wave's incidence angle effect on local & whole-body SAR [CHG+10], that most of the power is absorbed by muscles for frequencies around 100 MHz [CHL+08], that SAR is highly variable with the plane wave amplitudes, phases and directions of arrival for multiple plane waves exposure [KCH+11b]. While providing insight for our study, these studies lack the near-field exposure conditions. The study of plane waves in near-field is problematic when considering that in the immediate region surrounding the antenna, the angular field distribution of the antenna is distance-dependent ([VBPG15] and section 2.2.1). Plane wave usage suggests that the same electric field is applied on all spots of the human body surface, but in near-field

the electric field is highly variable, and cannot be represented by uniform plane waves. Additionally, plane waves require orthogonality between electric and magnetic fields, which is not always the case in near-field ([VBPG15] and section 2.2.1).

A plane wave expansion method exists to describe any wave using multiple plane waves [Goo05], but will not be used in this study because highly variable wave fields would need a high number of plane waves to be accurately represented, which increases the number of the necessary expansion modes, which in turn will increase the complexity of the computation.

2.2.3 Analysis of studies in near-field

Multiple papers studied near-field exposure to cell phones [HLD+05, WHWB08, KHS+16, KHV+17, MFE+17, LPH+19]. These studies were performed with mobile phones antennas. Because of the differences in frequencies, near-field exposure situations, and antenna size, none of the results obtained from cell phone near-field exposure can be used to assess workers' near-field exposure to FM, DAB or any base-station antenna radiation.

One study examined the impact of near-field emissions from a half-wave dipole antenna on human exposure [FD09] by performing SAR simulations with one emitter placed at various distances and heights. While providing local and global SAR values for reference, this study does not reflect the complexity of occupational environments, in which workers are exposed to EMFs from multiple sources including the reflections and diffractions caused by the metallic structure of FM masts.

One study [GVK+11] looked at human exposure to generic base station antennas mimicking real base stations in near-field. The paper provided estimation formulas for radiative near-field, but not for the reactive near-field due to the strong dependence of the localized absorption on the human anatomy, so the estimation formulas cannot be used to assess exposure for humans closer than 200 mm to base station antennas. Furthermore, this study assumed near-field conditions based on the well-known far field formula $r \geq \frac{2D^2}{\lambda}$, which is incomplete on its own as seen in section 2.2.1. Last, this study assumed exposure to the main beam in front of the antenna, which is different from exposure inside transmission pylons.

Studies with well-defined sources presented in this section offer accurate results but are complex to extrapolate to other configurations, especially with regards near-field characteristics.

2.3 Conclusion

Near-field exposure to FM antennas was studied with human models in fixed positions without taking into account the high variability of EMFs that occurs in near-field configurations. In human exposure, the worst case scenario approach in which SAR is studied where electric field is the highest, combined sometimes with statistics on a number of exposure cases is often the privileged methodology. The numerous exposure configurations in near-field in the literature, from plane waves to real on-site full-wave exposure, and the study of standards ICNIRP and IEEE in section 2.1.2, express the need for a generalized exposure assessment methodology, which is the goal of this work.

A near-field generator based on randomly positioned dipoles, each with random intensity, phase shift, and tilt will be used to recreate the near-field EMFs inside pylons. The steel lattice of FM transmission pylons causes EMFs to be reflected and currents are induced in the lattice itself, which makes the metallic structure a sum of indirect sources, hence exposure inside pylons is made of direct and indirect reflected EMFs from FM antennas, thus justifying the near-field generation choice. The near-field EMF exposure methodology will be explained first then validated using FM exposure simulations. Next, local and whole-body SAR results will be exposed and discussed. Finally, SAR surrogate models for workers' near-field exposure will be given.

Chapter 3

Near-field EMF exposure assessment: methodology

3.1 Introduction

3.1.1 Overall strategy

The overall strategy of this work is to divide the problem into two different domains, which are field generation and human exposure. The field generation will focus on recreating the EMFs that can be encountered in existing pylons and extending the available pool of EMFs by creating new EMFs that have similar characteristics as those that can be found in real situations. The human exposure assessment consists of FDTD simulations to calculate SAR in any exposure situation. By separating an exposure problem into field generation and human exposure, the SAR assessment results will be generic and not specific to a particular exposure situation, but with specific EMF characteristics.

Previous studies (section 2.2) linked SAR exposure to specific sources. To overcome this problem, random incident fields were used in this work's methodology. The general idea is to generate random incident fields that have similar near-field characteristics as those that can be found in the reference fields, which are real pylons EMFs reproduced using simulation. The randomness of the incident fields guarantees the absence of relationship between a near-field assessment and a specific antenna or source.

In order to ensure the generalization of the methodology to all exposure cases, millions of random incident fields will be generated. They will not all be subjected to time-consuming SAR assessments, but a random choice of a limited number of cases will be assessed using SAR.

Initially, random incident fields will be generated by assuming there are no interactions between incident fields and the human model. Therefore, the human model will be exposed to incident fields with certain characteristics that were not obtained in FM pylons, but that are similar as those found in FM pylons. The use of the equivalent principle will make it possible to expose a human model to any random incident fields. The exposure assessment will be done using SAR and a Huygens box, which is detailed in the next chapter.

3.1.2 Methodology introduction

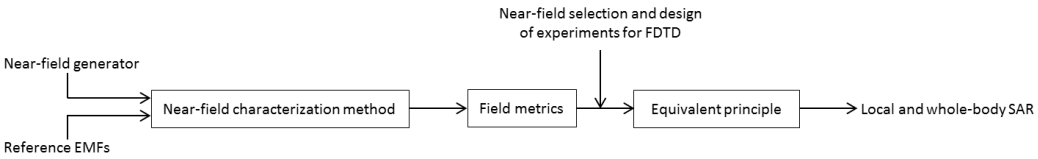

Figure 3.1: Block diagram of the used methodology.

The study will look into occupational exposure induced by one or multiple FM emitters in transmission pylons, which will be called reference EMFs. A near-field generator provides EMF similar to those that can be found in the transmission pylons, which will be called generated EMFs. Both reference and generated EMFs will be used with the near-field characterization method to find which near-fields should be used for SAR assessment. The block diagram in figure 3.1 shows an overview of the entire methodology. The near-field EMF exposure assessment methodology studies EMF characteristics rather than source characteristics, thus removing the necessity of knowing antenna power, gain and whether there is coupling between different sources.

3.2 Methodology

3.2.1 Random field generation through multiple dipole combinations

Multiple dipoles combinations

In order to recreate the highly variable near-field inside transmission pylons, multiple infinitesimal dipoles are used. The total electric and magnetic radiation of multiple dipoles is computed in a given volume. Each dipole is computed using the descriptive equations for the E and H fields, as show in

3.1, given by reference [Bal16].

$$\begin{aligned} E_r &= \eta \frac{I_0 l \cos\theta}{2\pi r^2}\left[1+\frac{1}{jkr}\right] e^{-j(kr+\psi)} \\ E_\theta &= j\eta \frac{kI_0 l \sin\theta}{4\pi r}\left[1+\frac{1}{jkr}-\frac{1}{(kr)^2}\right] e^{-j(kr+\psi)} \\ E_\phi &= 0 \\ H_r &= H_\theta = 0 \\ H_\phi &= j \frac{kI_0 l \sin\theta}{4\pi r}\left[1+\frac{1}{jkr}\right] e^{-j(kr+\psi)} \end{aligned} \tag{3.1}$$

where η is the wave impedance of the medium, $k = 2\pi/\lambda$, r is the distance from source to observation point, I_0 is the dipole amplitude in amperes, l is the dipole length, ψ is the phase of the signal radiated by the dipole. Equations 3.1 are then converted from polar to cartesian coordinates, and two rotation angles (θ_o,ϕ_o) corresponding to the orientation angles of the dipole are applied. Figure 3.2 shows an infinitesimal dipole in its initial state.

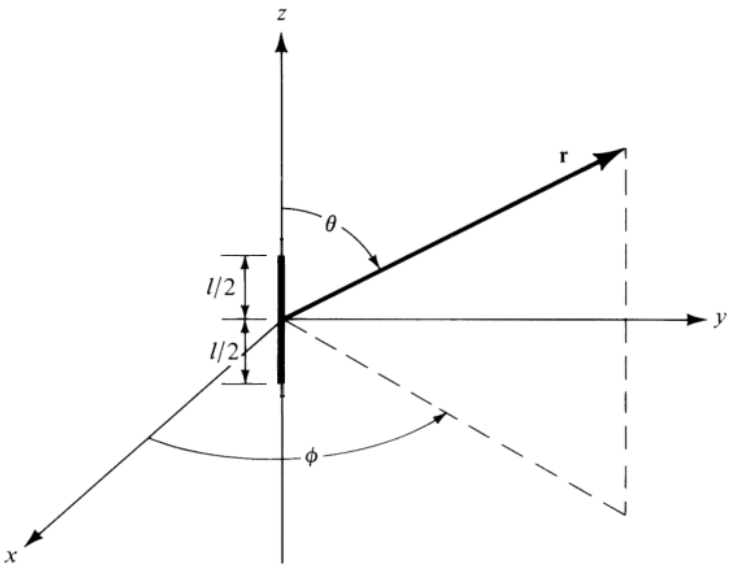

Figure 3.2: Infinitesimal dipole in the initial state [Bal16].

Each dipole has therefore 7 different inputs: amplitude I_0, phase ψ, 2 orientation angles (θ_o,ϕ_o), 3 position coordinates (x,y and z in Cartesian coordinates). Amplitude and phase are related to the source description, whereas the remaining 5 inputs are related to dipole position and tilt. All inputs can be assigned randomly in order to generate a near-field with the right characteristics. This near-field generation technique allows degrees of freedom multiple of the number of placed dipoles. Figure 3.3 shows an example of dipoles distribution and orientations around a characterization volume representing a phantom.

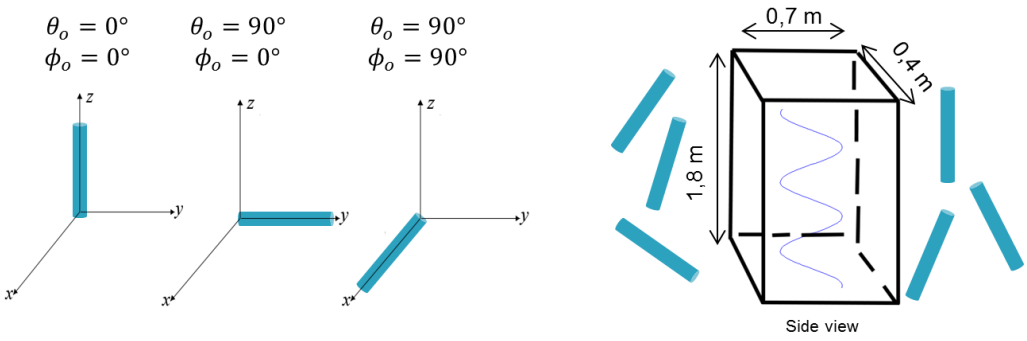

Figure 3.3: On the left, dipoles with different orientation angles. On the right, dipoles are placed around the human characterization volume.

The simplicity of the dipole description allows for fast simulations and allows the modification of known physical parameters such as the amplitude or position of the dipole. This would not have been possible with the plane wave expansion method, since it relies on mathematical descriptions with no physical parameters. The spherical wave expansion would require the use of complex modes in a mathematical description in a random fashion. For these reasons, we chose to use infinitesimal dipoles.

E- and H-field components in equations 3.1 are valid on any point except on the source itself, provided that the infinitesimal dipole is small ($l << \lambda$) and very thin ($a << l$).

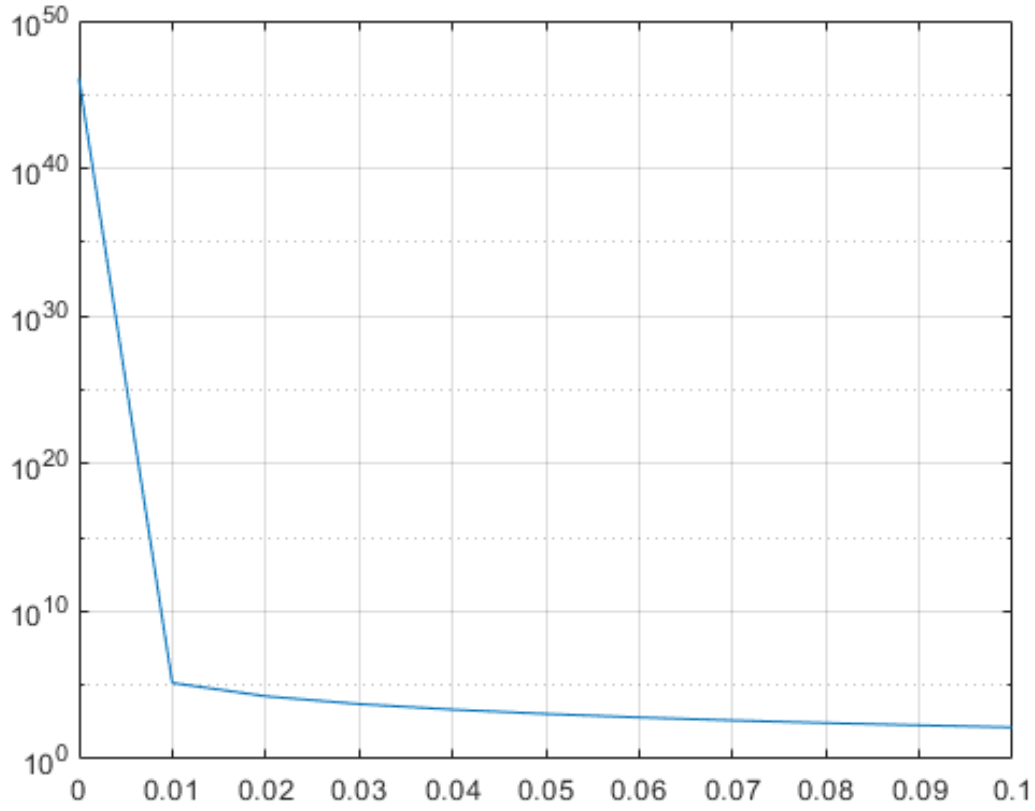

Figure 3.4: Electric field (in V/m) vs distance (in meters) for one infinitesimal dipole, computed using equations 3.1. *Amplitude* = 1 A, l = 1 cm, f = 100 MHz.

Limitations

Equations 3.1 are extracted from reference [Bal16], which specifies that the radiated fields equations are valid everywhere, except on the source itself. We show that equations 3.1 cannot be used in the very near-field. Figure 3.4 shows that in the very near-field (1 to 5 cm) of a single 1 cm dipole at 100 MHz, the electric field value decreases from 1.4×10^5 V/m to 1.1×10^3 V/m, which is physically impossible because a single 1 cm dipole cannot emit such powerful field strengths. Equations 3.1 must therefore be used at a certain minimal distance from the probe point, which will be determined when a reference can be defined. These limitations are inherent to equations 3.1.

3.2.2 EMF numerical calculations for reference

64 entire pylons or sections of pylons, equipped with FM antennas, were modelled using CST Microwave Studio, an EMF simulation software. Models included steel lattice masts, steel ladders, platforms, and the FM antennas. Most antennas were single dipoles placed on the transmission tower. In other cases, antenna arrays with multiple dipoles and reflector were placed at different height on the same pylon. Pylons models include 10 existing pylons used by European broadcasting companies, as well as 54 generic pylons that are simplified versions of what broadcasting companies can use in reality.

Electric and magnetic fields emitted inside the pylons were computed then extracted with a 2 mm grid. We will study EMF by looking at the places where workers are expected to intervene inside the pylons. This includes all EMFs inside the steel lattice, provided these EMFs are no further than 1.5 m from the extremity of the emitters, so as to remain in the near-field of the emitters. Near-field conditions will be verified using field metrics explained later. The field metrics will serve as a base reference for the rest of our study, as they will allow us to validate the near-field exposure assessment methodology. All near-fields that are close to reality by fitting the required field metrics will be added to a reference bank of verified near-fields, as they will serve as reference. Having such a reference can limit the number of exposure scenarios in near-field, since the number of studied pylons is limited to 64. Our goal is therefore to provide a larger number of simulated random cases than those found in the near-field reference.

3.3 Near-field characterization method: field generation fitting

3.3.1 Introduction

The near-field generator (section 3.2.1) provides 7 degrees of freedom per dipole, with the 8th degree of freedom being the number of dipoles. The use of a large number of dipoles is required to generate incident near-fields similar to fields found in pylons. All dipoles are randomly placed around a characterization volume (e.g. figure 3.5), which has the same size as a human volume. Dipoles are made to face the human volume without being

inside the characterization volume. Their amplitudes, phases and tilts are also randomly assigned. Field metrics are then calculated inside the human volume, using the EMFs resultant from the near-field generator.

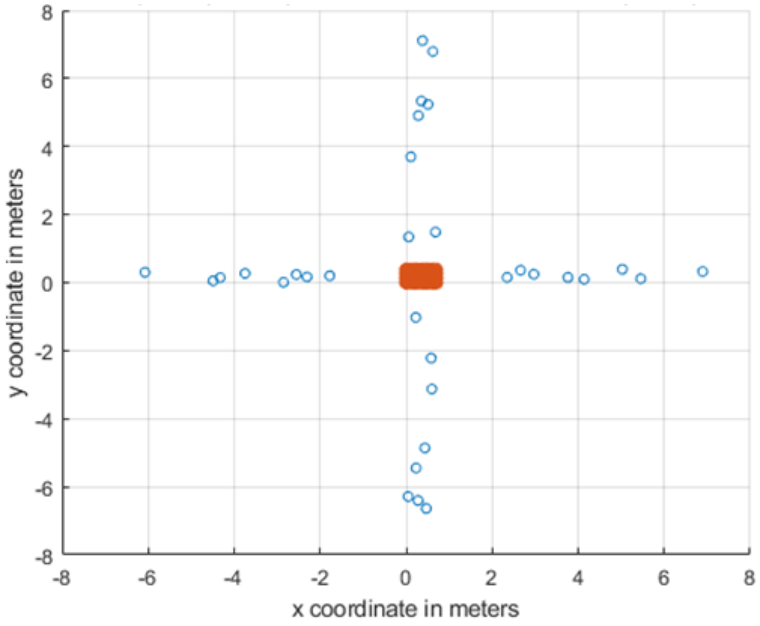

Figure 3.5: Infinitesimal dipoles (empty circles) randomly placed around a characterization volume (filled rectangle in the middle), seen from above. Distances are in meters.

3.3.2 Simulation process

Each new simulation using the near-field generator requires setting dipole inputs to random values. Since the number of variables depends on the number of dipoles, a large number of dipoles means a larger number of inputs. In our case, the near-field generator has $7 \times n_d$ inputs, with n_d being the number of dipoles. In order to accurately represent near-field radiation in the reference pylons, we plan to use 8 dipoles facing each lateral side of the human volume (figure 3.5 shows one example of dipoles placed to face the lateral sides of the human volume, in a cross fashion as shown in the figure). In total, 32 dipoles in total are placed around the human volume, together they amount to 224 inputs for a single simulation giving electric and magnetic

fields as outputs. The computation process used is Monte Carlo simulations, whereby a large number of random variables are drawn for each input and simulations are performed for millions of times until the output is accurately predicted. For each input, 1 million variables are drawn following Latin Hypercube sampling [MBC79] coupled with a "maximin" criterion to maximize the minimum distance between points, in order to optimize the number of turns needed to predict the ouput behaviour.

The resulting electric and magnetic fields outputs from each new simulation need to be compared to the results found in the reference pylons. Since 224 inputs result in 2 outputs (which are the electric and magnetic fields), it is difficult to predict what interactions between the inputs causes a variation in the ouputs. Therefore, SAR will be linked to the near-field generator outputs, which is less difficult than predicting which of the 224 inputs causes a SAR variation. This works proposes a field metrics assessment technique in which the outputs from the generated field metrics (GFM) will be compared to reference field metrics (RFM) obtained from reference pylons.

3.3.3 Field metrics assessment

The near-field environment studied in pylons can be either in the reactive or the radiative field zones. Due to the difficulties related to near-field presented in section 2.2.1, field metrics for field discrimination must be defined. Field metrics will serve as a mean of comparison between reference and generated fields (see sections 3.2.1 and 3.2.2 respectively). Field metrics will therefore need to assess near-field characteristics and exposure.

It was shown in section 2.2.1 that 2 criteria can be used as near-field characteristics: the angles formed between E and H fields ($\widehat{E,H}$) at the same location, and the wave impedance ratio $\frac{E}{H}$. Additional field metrics for exposure assessment are needed. Two field metrics can be used for exposure assessment: field strength ratio ($\frac{E_{max}}{E_{avg}}$), and maximum electric field concentration $c(E)$.

The field strength ratio $\frac{E_{max}}{E_{avg}}$ in which E_{max} is the maximum electric field spatially averaged over a $512 - \text{cm}^3$ cube ($8 - \text{cm}$ side length) so as to mimmick a field probe, and E_{avg} is the electric field spatially averaged over the

Field metric	Mathematical expression	Use
Maximum to average field ratio	E_{max}/E_{avg}	Exposure assessment
Concentration around the maximum E field value	$c(E)$	Exposure assessment
Field wave impedance	E/H	Near-field assessment
Angles between electric and magnetic fields	$(\widehat{E,H})$	Near-field assessment

Table 3.1: Field metrics.

entire human volume with a 1-cm step. This criterion will help us study the relationship between local SAR (SAR_{10g}) and E_{max}. The maximum electric field concentration $c(E)$ is defined as the distance between E_{max} and $0.9 \times E_{max}$ in the human sized volume. This criterion will allow us to identify the link between SAR and field concentration.

$\frac{E}{H}$ and $(\widehat{E,H})$ field metrics are related to the near-field nature of the incident fields, and satisfy plane wave conditions in far-field. Field strength ratio and concentration around maximum electric field were defined in this work as field metrics for exposure assessment. All field metrics are calculated in human volumes sized 0.4m $\times$ 0.7m $\times$ 1.8m, which is the volume of the phantom used for SAR assessment (section 4.3.1).

Using field metrics for near-field characterization ($(\widehat{E,H})$ and $\frac{E}{H}$) allows us to compare reference and generated field metrics. While not providing the exact field region in which the measurement is performed, such an assessment is valuable to generate new cases of exposures that are pertinent. Field metrics for exposure assessment ($\frac{E_{max}}{E_{avg}}$ and $c(E)$) quantifies how greater is E_{max} in comparison to E_{avg} and $c(E)$ evaluates the concentration around E_{max}. High $\frac{E_{max}}{E_{avg}}$ and $c(E)$ values are expected to correlate with the location of localized maximum SAR (SAR_{10g}). Table 3.1 summarizes field metrics and their use. Figure 3.6 shows an overview of the near-field generator with inputs and outputs.

In order to illustrate the random field generation and the field metrics assessment working together, an example is given on figures 3.7 and 3.8, along with table 3.2. Dipoles were randomly placed around the characterization volume, in such a way that they always face said volume, as it can be seen on figure 3.7. The electric field was calculated and given on figure 3.8 for a single plane. The field metrics were calculated and given on table 3.2.

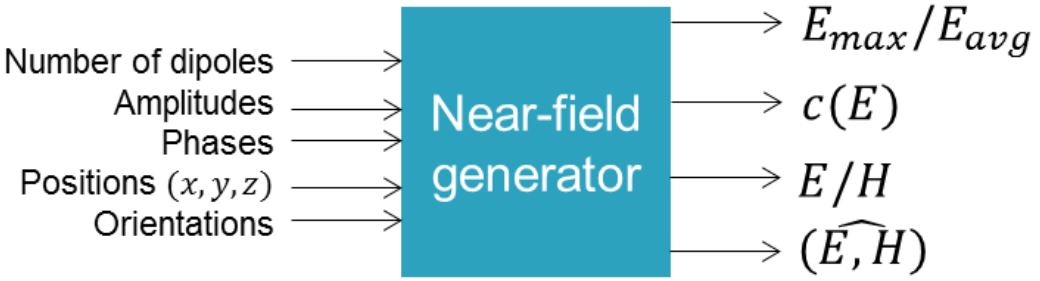

Figure 3.6: Overview of the near-field generator with inputs and outputs.

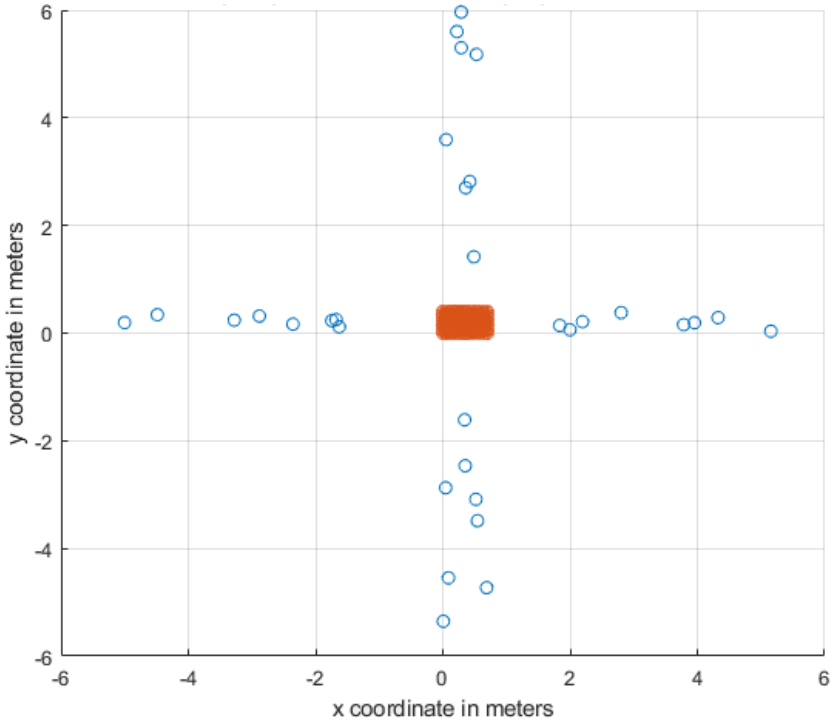

Figure 3.7: Use case: dipoles placement (blue empty cirles) around a human volume (red rectangle in the middle). E field is calculated and provided on figure 3.8.

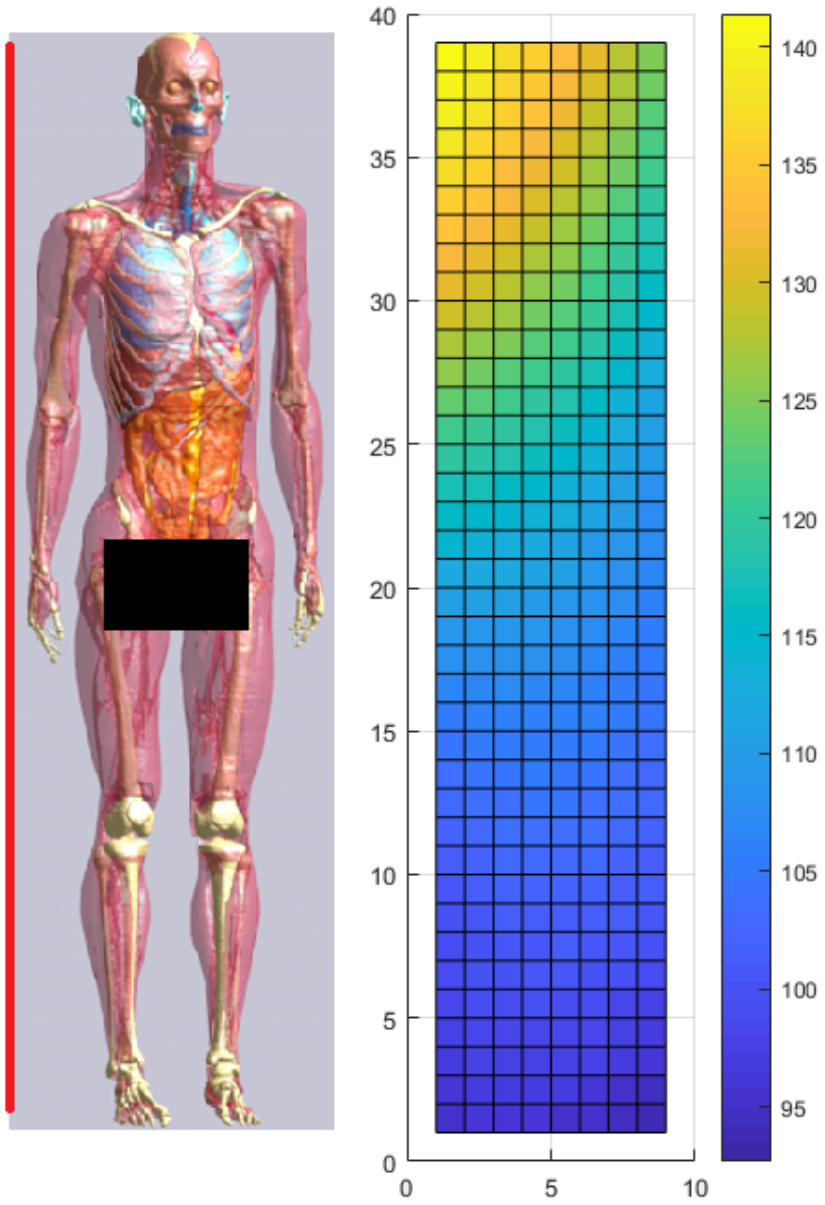

Figure 3.8: Use case: E field calculated in V/m at plane $x = 0$ m, front of human model, for dipoles placed such as indicated in figure 3.7. The human model is shown on the left, with a vertical red line showing the plane surface map where E is calculated. One division is 5 cm. Table 3.2 shows field metrics calculated for this use case.

Field metric	Value
E_{max}/E_{avg}	1.42
$c(E)$	0.81 m
E/H	258 Ω
$(\widehat{E,H})$	0.68 rad

Table 3.2: Use case: field metrics. See figure 3.7 for dipoles placement and figure 3.8 for E field calculation.

3.3.4 Sensitivity analysis and near-field generation

Motivations

The near-field generator 3.2.1 has 224 inputs and 4 outputs, which are the field metrics defined in 3.3.3. It is necessary to perform sensitivity analysis to understand how the inputs affect the outputs. Various sensitivity analysis exist in the literature [BP16]. The goal is to quantify the effect of each input on outputs. Hence for our purposes, variance-based techniques are the most appropriate, namely Sobol indices for senstivity analysis [IM93]. The results from Sobol indices will be discussed then implemented to find other trends and patterns.

Sobol indices

Method Suppose a model function $Y = f(X_1, X_i, ..., X_n)$ where X_i is the i-th input ($i\epsilon\,[1, n]$) and Y the output. The first order effect sensitivity index is defined as

$$S_i = \frac{Var[E[Y|X_i]]}{Var[Y]} \tag{3.2}$$

The total sensitivity effects are written

$$ST_i = \frac{Var[E[Y|X_{\sim i}]]}{Var[Y]} \tag{3.3}$$

where $X_{\sim i} = (X, ..., X_{i-1}, X_{i+1}, ..., X_n)$ is the parameter combination complementary to X_i.

The first order effects in equation 3.2 show the main effects of X_i on the output, whereas the total effects index 3.3 measures the effects of interactions

between all inputs on the output. Equations 3.2 and 3.3 were implemented using reference [Bil14], to study the effects of the near-field generator inputs on the outputs, as shown in figure 3.6. Monte Carlo simulations with 1 million trials were performed to find the Sobol indices of each input. The results can be seen on figures 3.9a to 3.9d.

Results Sobol indices for first order effects show little difference between position coordinates (x, y, z), orientation angles $(theta, phi)$, phase and amplitude. Dipole position coordinates (x, y, z) and dipole orientation angles were summed together to identify trends more easily. Dipole position coordinates are the largest Sobol index, followed by dipole orientation angles. This is true for all 4 outputs in figure 3.6.

Sobol indices for total effects however show a different behavior, depending on the output. When considering E_{max}/E_{avg}, it can be seen that position coordinates make up for 90 % of the impact on output variance, which means that there are interactions between x, y, z , and amplitude to a lesser degree. For E/H, $c(E)$ and $(\widehat{E, H})$, it can be seen that the mutual interactions between dipole position and orientation angles make up for 70 % of the impact on variance. Phase and amplitude are not negligible, but their impact on the variance is limited to the remaining 30 %.

To conclude, sensitivity analysis of Sobol indices show that dipole position and orientation have the most impact on the outputs.

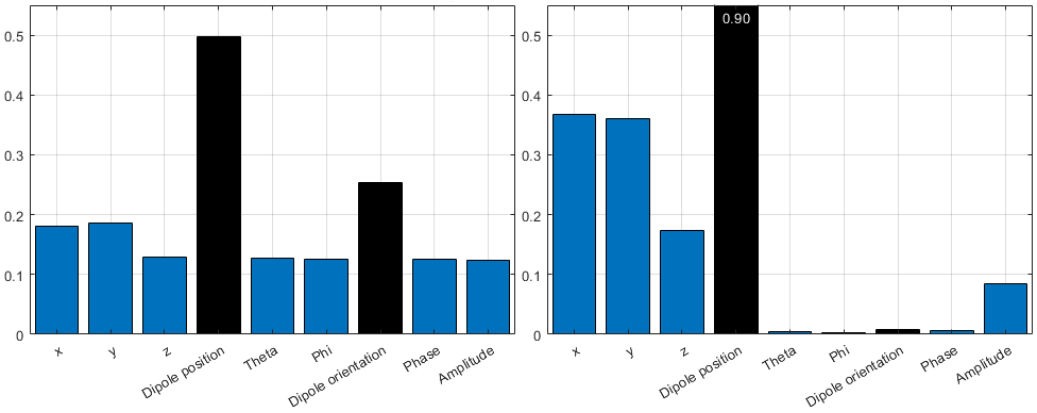

(a) Sobol's indices of different inputs impact on E_{max}/E_{avg}. First order effects (left) and total effects (right).

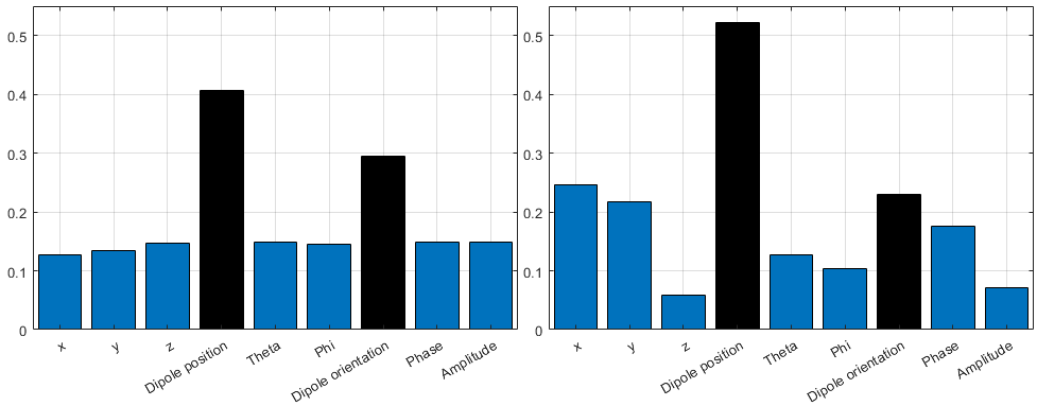

(b) Sobol's indices of different inputs impact on E/H. First order effects (left) and total effects (right).

Figure 3.9: Sobol's indices showing the impact of each input on E_{max}/E_{avg} and E/H.

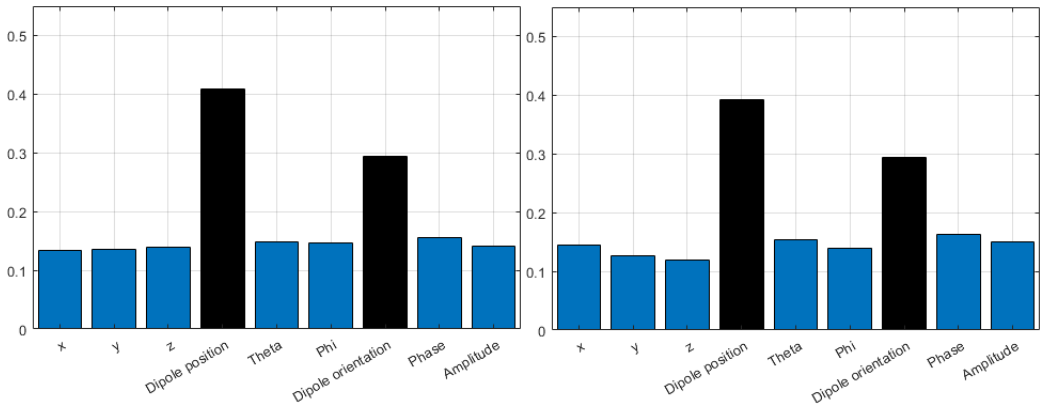

(c) Sobol's indices of different inputs impact on $c(E)$. First order effects (left) and total effects (right).

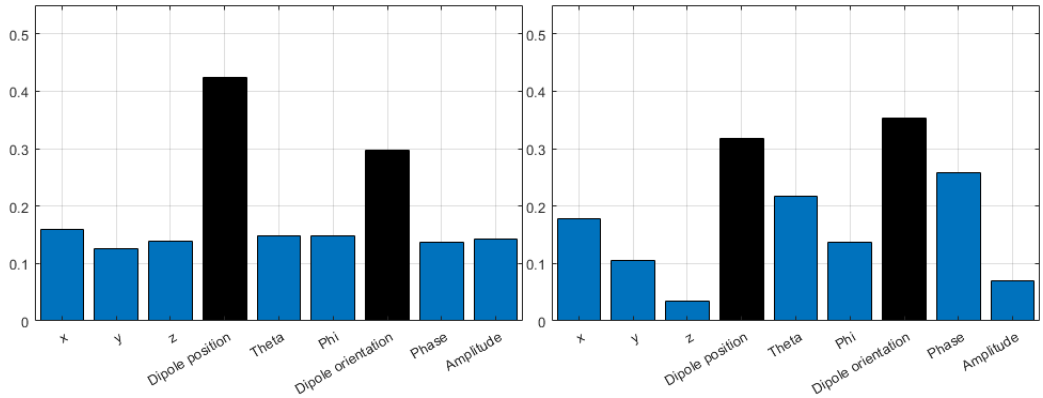

(d) Sobol's indices of different inputs impact on $(\widehat{E,H})$. First order effects (left) and total effects (right).

Figure 3.9: Sobol's indices showing the impact of each input on $c(E)$ and $(\widehat{E,H})$.

Sensitivity analysis using random simulations

Sobol indices have shown in 3.3.4 that dipoles' positions make up on average for 40 % of the impact on the outputs' variance. Dipole position coordinates translate into distances between dipole position and the human volume (example on figure 3.5). Dipoles' position coordinates x_i, y_i, z_i (i designating the i-th dipole) can be used to calculate the distance r from characterization

volume (human volume) to dipole

$$r = \sqrt{(x_{HVc} - x_i)^2 + (y_{HVc} - y_i)^2 + (z_{HVc} - z_i)^2} \tag{3.4}$$

where $x_{HVc}, y_{HVc}, z_{HVc}$ designate the characterization volume (CV) center. Since distances from dipoles to CV are the most impactful, minimal and maximal distances from CV to dipole must be chosen carefully.

The other most impact result is dipoles' orientation angles θ and ϕ, which were defined in figure 3.3. Sobol indices show that orientation angles make up for up to 30% of the impact on the outputs' variance.

Method: impact of dipoles position coordinates on field metrics distributions In order to measure the impact of dipole position coordinates, only dipoles positions were varied while the rest of the inputs are set to fixed range values. The observed outputs are the probability density functions (PDFs) of the 4 field metrics (E_{max}/E_{avg}, $c(E)$, E/H, and $\widehat{(E,H)}$). The PDFs are assimilated to a known PDF, likely a Normal or an Inverse Gaussian distribution.

Figure 3.10 shows a dipole exposure configuration with 32 randomly placed dipoles, 8 per lateral side of CV. It can be seen that dipoles are facing the CV (explanation in section 3.2.1). Exclusion zones are shown, and designate zones where dipoles are not placed. Additionally, to take into account the distance between dipoles and CV, $d_{min\,x}$ and $d_{min\,y}$ were defined as the minimal distances from dipoles to CV, d_{max} as the maximal distances of dipoles. All of the distances are indicated clearly on figure 3.10. The impact of both d_{min} and d_{max} are measured separately.

On figure 3.10, we identified minimal distances $d_{min\,x}$ and $d_{min\,y}$ which indicate the minimal distance between any of the dipoles and the nearest characterization volume boundary. When performing the simulation, both $d_{min\,x}$ and $d_{min\,y}$ were given the same values so that $d_{min} = d_{min\,x} = d_{min\,y}$. the results can be seen on figure 3.11. The inputs were summarized in table 3.3. The impact of d_{max} on the field metrics distributions is measured by setting the near-field inputs as shown in table 3.4.

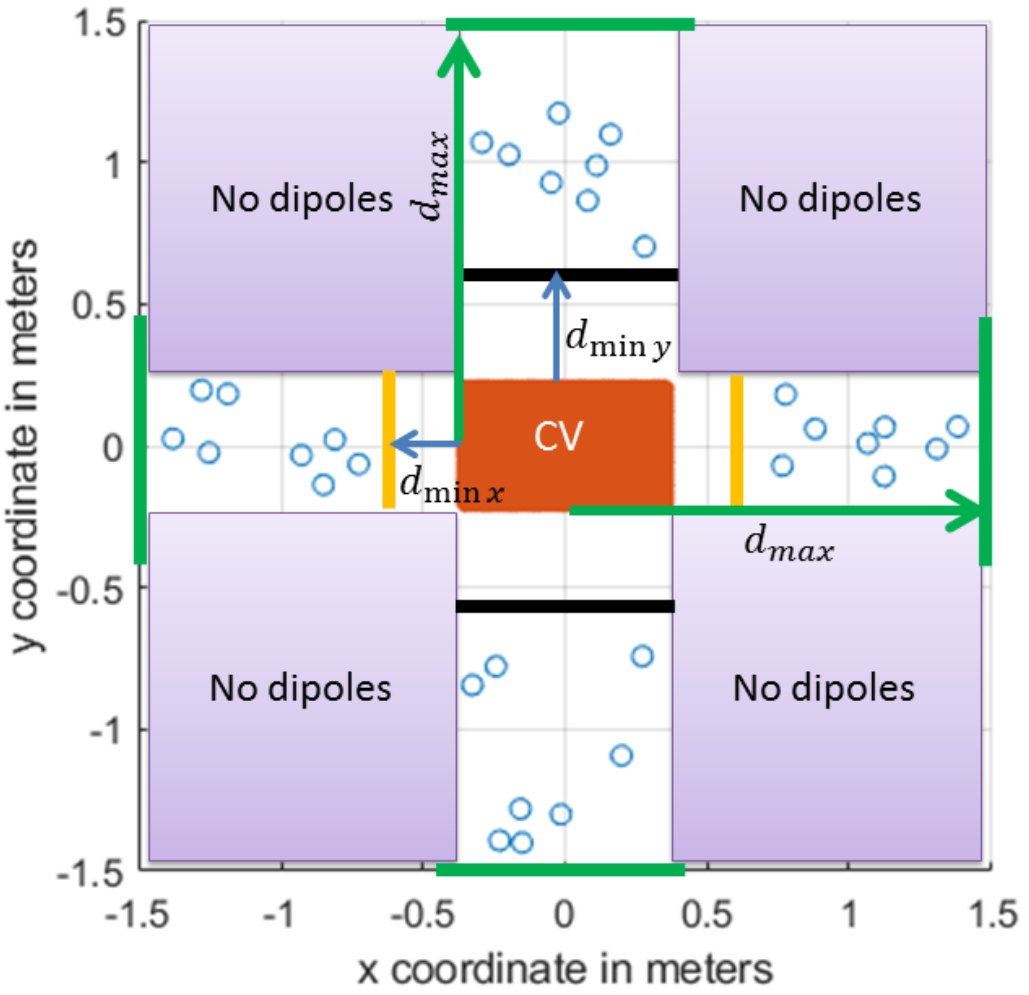

Figure 3.10: Dipoles (empty blue circles) and characterization volume (red rectangle in the center). Pictured from above the characterization volume.

Inputs	Range [min - max]
Number of dipoles	32
Amplitude	$[0 - 0.5$ A$]$
d_{max}	6 m
d_{min}	0.1 m or 0.5 m or 0.9 m
Phase	$[0 - 2\pi]$
Orientation θ	$[0 - 2\pi]$
Orientation ϕ	$[0 - 2\pi]$

Table 3.3: Inputs for simulations performed on figure 3.11 to find the impact of d_{min} on field metrics distributions.

Inputs	Range [min - max]
Number of dipoles	32
Amplitude	$[0 - 0.5$ A$]$
d_{max}	2 m or 4 m or 7 m
d_{min}	0.15 m
Phase	$[0 - 2\pi]$
Orientation θ	$[0 - 2\pi]$
Orientation ϕ	$[0 - 2\pi]$

Table 3.4: Inputs for simulations performed on figure 3.12 to find the impact of d_{max} on field metrics distributions.

Results

Minimum distance effects It can be seen on figure 3.11 and table 3.5 that d_{min} causes an impact on all parameters, except the first parameter of the angles normal distribution. The impact on both $Emax/Eavg$ and E/H is non-negligible. d_{min} has an important impact on the field metrics distributions.

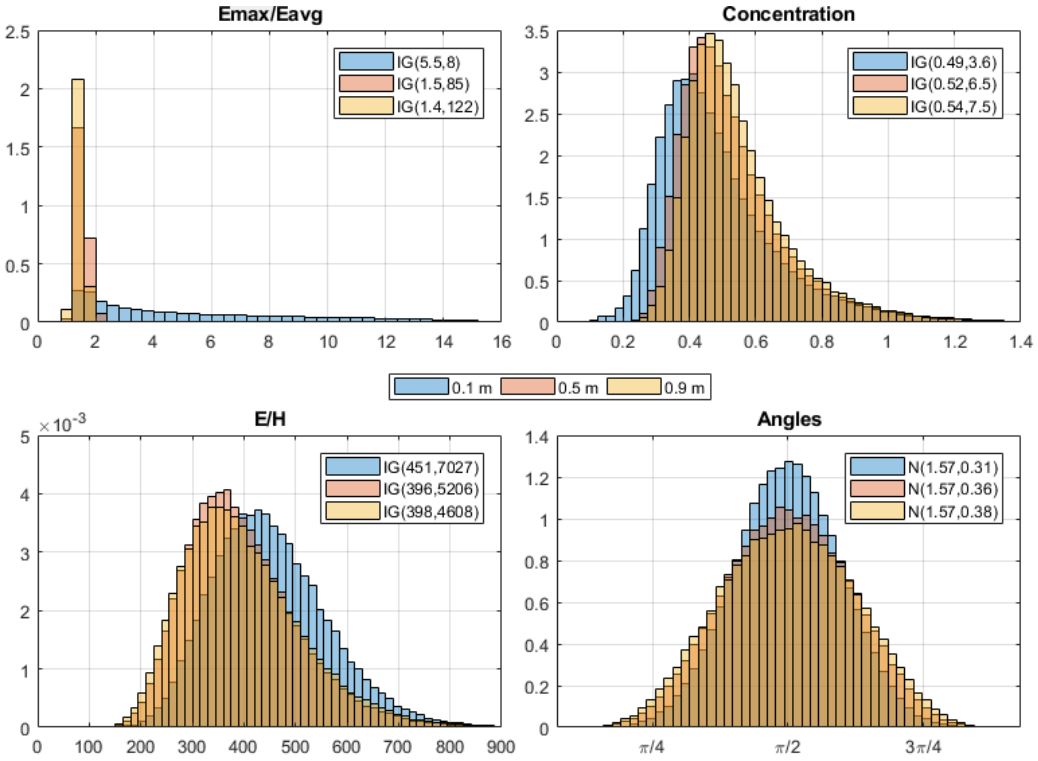

Figure 3.11: Field metrics distributions. Simulation were performed with all inputs set randomly (see table 3.3). Minimum distances were set to one of the following: 0.1, 0.5 and 0.9 m.

Field metric	Best fitting distribution	Impact on first parameter	Impact on second parameter
E_{max}/E_{avg}	Inverse Gaussian	-290%	1425%
$c(E)$	Inverse Gaussian	10%	108%
E/H	Inverse Gaussian	-12%	-34%
$(\widehat{E,H})$	Normal	0%	22%

Table 3.5: Percentage difference between distribution parameters for minimum and maximum d_{min}. Results for simulations performed on figure 3.11 to find the impact of d_{min} on field metrics distributions.

Maximum distance effects d_{max} causes an impact on all parameters, except the first parameter of the angles normal distribution. It is shown by table 3.6 that the most impacted distribution is the E_{max}/E_{avg} PDF.

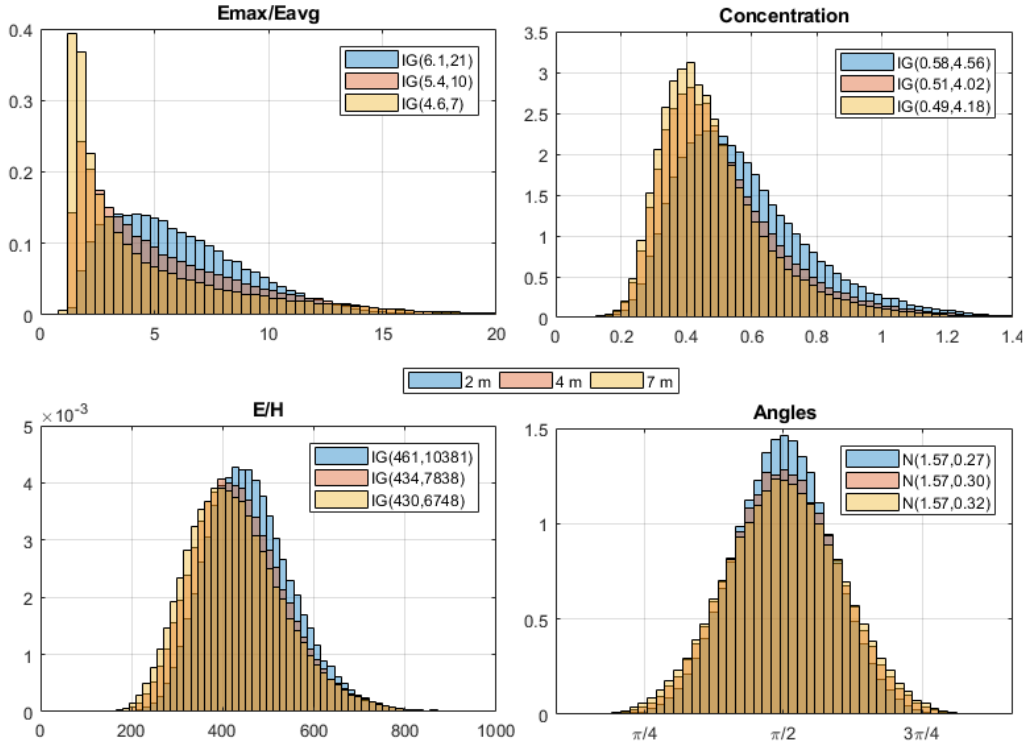

Figure 3.12: Field metrics distributions. Simulation were performed with all inputs set randomly (see table 3.4). Maximum distances were set to one of the following: 2, 4 or 7 m.

Method: impact of dipoles orientation angles on field metrics distributions The Sobol indices of the orientation angles of dipoles were shown to have an impact on all outputs except field strength ratio (E_{max}/E_{avg}) total effects (see figure 3.9). In order to measure the impact of dipole orientation angles, only orientation angles were varied while the rest of the inputs were set to fixed range values. The observed outputs are the probability density functions (PDFs) of the 4 field metrics (E_{max}/E_{avg}, $c(E)$, E/H, and $(\widehat{E,H})$). The PDFs are assimilated to a known PDF, likely a Normal or an Inverse Gaussian distribution.

Field metric	Best fitting distribution	Impact on first parameter	Impact on second parameter
E_{max}/E_{avg}	Inverse Gaussian	-24%	-67%
$c(E)$	Inverse Gaussian	-16%	-67%
E/H	Inverse Gaussian	-7%	-35%
$(\widehat{E,H})$	Normal	0%	19%

Table 3.6: Percentage difference between distribution parameters for minimum and maximum d_{max}. Results for simulations performed on figure 3.12 to find the impact of d_{max} on field metrics distributions.

For each dipole, orientation angles θ_o and ϕ_o were set randomly, their values range from 0 to 2π. Table 3.7 shows the inputs of the experiment. The design of the experiment is shown on table 3.7.

Inputs	Range [min - max]
Number of dipoles	32
Amplitude	$[0 - 0.5$ A$]$
d_{max}	6 m
d_{min}	0.20 m
Phase	$[0 - 2\pi]$
Orientation θ	0 or $[0 - 0.25\pi]$ or $[0 - 2\pi]$
Orientation ϕ	0 or $[0 - 0.25\pi]$ or $[0 - 2\pi]$

Table 3.7: Inputs for simulations performed on figure 3.13 to find the impact of dipole orientation θ and ϕ on field metrics distributions.

Results of dipoles' orientation angles on field metrics distribution Dipoles orientation angles have little impact on E_{max}/E_{avg}, $c(E)$, and E/H field metrics distribution, as shown by table 3.8. The only impact of dipoles orientation angles is on the angles PDFs. The increase of the orientations range causes a 167% increase on the second parameter of the normal distribution.

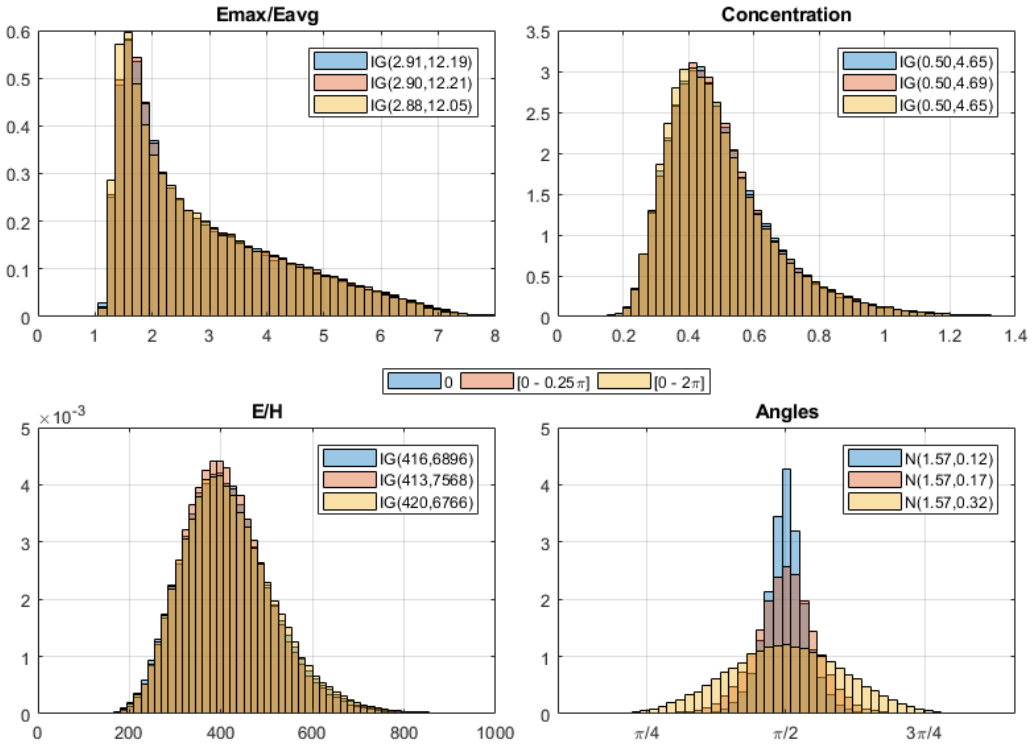

Figure 3.13: Field metrics distributions. Simulation were performed with all inputs set randomly (see table 3.7). Orientation ranges were set to one of the following: 0, $[0 - 0.25\pi]$ or $[0 - 2\pi]$.

Field metric	Best fitting distribution	Impact on first parameter	Impact on second parameter
E_{max}/E_{avg}	Inverse Gaussian	-1%	-1%
$c(E)$	Inverse Gaussian	0%	0%
E/H	Inverse Gaussian	1%	-2%
$(\widehat{E,H})$	Normal	0%	167%

Table 3.8: Percentage difference between distribution parameters for minimum and maximum orientation angles. Results for simulations performed on figure 3.13.

Conclusion

Dipole position coordinates and more precisely d_{min} and d_{max} are the most impactful inputs, and will be used to find the most fitting generator field

metrics (GFM) to the reference field metrics (RFM). All simulations with the near-field generator will focus on d_{min} and d_{max} as the primary inputs to impact field metrics distributions.

The results show that dipoles' orientation angles should be considered to find the correct angles $(\widehat{E,H})$ field metric PDF, if d_{min} and d_{max} do not suffice on their own to find the correct $(\widehat{E,H})$ metrics distribution.

3.3.5 Design of experiments for field generation

Since the goal is to reproduce the behavior of EMFs observed inside pylons, trials using the near-field generator must be performed following a design of experiments (DoE). The DoE will include variations of d_{min} and d_{max} until the appropriate values for both are found. d_{min} and d_{max} can only be defined when generated field metrics (GFM) are compared to reference field metrics (RFM). All inputs values are chosen using a random uniform draw, within certain boundaries. 80 different scenarios called $GFM1$ to $GFM80$ are tested and presented in this study, where dipoles tilts and phases are chosen randomly from 0 to 2π, amplitudes from 0 to 0.5 A and dipoles' heights (z coordinate) from 0 to 1.7 m. The only varying boundaries are distances d_{min} and d_{max}, they are chosen randomly from 0 to 0.35 m with a 0.05 m step for d_{min}, 1 to 10 m with a 1 m step for d_{max}. Table 3.9 shows some of the experiments that will be conducted.

Scenario	d_{min} in meters	d_{max} in meters
GFM 1	0.05	1
GFM 2	0.05	2
GFM 3	0.05	3
...	...	...
GFM 79	0.70	9
GFM 80	0.70	10

Table 3.9: Design of experiments for the near-field generator simulations, with the different GFM scenarios.

3.4 Conclusion

Chapter 3 presented the near-field EMF exposure methodology by showing the overall strategy, the methodology based on field metrics, and characterization method used in this work. The near-field generator and the pylons simulations were presented, as they are the basis of this work. The near-field generator was characterized, and a sensitivity analysis was performed. Last, a design of experiments for field generation was defined and will be used in the next chapter.

Chapter 4

Near-field EMF exposure assessment: material and validation

4.1 Introduction

In the last chapter, the reference and generated field metrics were defined. Sensitivity analysis was performed on the near-field generator to better understand how it works. In this chapter, near-field exposure assessment methodology is validated by detailing field metrics collection, assessment, and control. The design of experiments of SAR simulations is discussed. The human exposure computation material is shown.

4.2 Near-field characterization method validation

4.2.1 Near-field characterization for human exposure: field metrics assessment and control

Field metrics collection and analysis

Field metrics are collected and stored in 2 different matrices that have the following format:

$$Field\ metrics_{id} = \begin{bmatrix} \frac{E_{max}}{E_{avg}}_1 & c(E)_1 & \frac{E}{H}_1 & \widehat{(E,H)}_1 \\ \frac{E_{max}}{E_{avg}}_2 & c(E)_2 & \frac{E}{H}_2 & \widehat{(E,H)}_2 \\ \dots & \dots & \dots & \dots \\ \frac{E_{max}}{E_{avg}}_n & c(E)_n & \frac{E}{H}_n & \widehat{(E,H)}_n \end{bmatrix} \tag{4.1}$$

where *id* defines if the *Field metrics* matrix is reference field metrics (RFM) or generated field metrics (GFM), and n is the total number of human volumes in a given environment. Field metrics are collected in a «human volume»sized 0.4m $\times$ 0.7m $\times$ 1.8m. There are 2 phases during the field metrics assessment and control: a first phase where results are collected from both RFM and GFM to be compared, and a second phase where choosen GFM are used for SAR simulations. Each phase will be detailed in a different paragraph to better understand the field metrics collection process.

Phase 1: field metrics collection for comparison The near-field generator becomes time-consuming when the field metrics collection is set to

a small resolution. To ensure fast simulations in the first phase, field metrics are calculated every $10-$ cm inside the human volume, which means 504 points are collected in each human volume. All field metrics are then averaged and stored in a single matrix (see matrix 4.1). RFM and GFM collection processes are explained in different paragraphs. The $10-$ cm resolution ensures small simulation time as well as reliable field metrics results for comparison.

Reference field metrics collection RFM are collected in all of the 64 modeled FM pylons 3.2.2. A human volume ($0.4\text{m} \times 0.7\text{m} \times 1.8\text{m}$) is slided from the bottom of a pylon to its top, with a $10-$ cm step. With each new height, the volume is also slided from side to side with a $10-$ cm step, so as to explore all places that could be accessed by a worker in reality, at a 1.5m maximum distance from the antenna arrays extremities. All field metrics are collected as in matrix 4.1. All pylons field metrics are then combined in a single matrix, which becomes RFM. In this study, RFM combined 3.9 million of cases, all taken from the 64 pylons. Figure 4.1 shows how human volumes move inside pylons.

Generated field metrics collection GFM are produced by exposing a human volume to randomly placed dipoles, as shown previously in figure 3.10. The human volume ($0.4\text{m} \times 0.7\text{m} \times 1.8\text{m}$) is averaged the same way as in pylons, with field metrics collected using a 10cm resolution. However, in this case, the human volume does not move, rather dipoles are placed differently and their inputs are changed with every new iteration. The number of iterations is 2 million to find the best fitting GFM in phase 2.

Phase 2: field metrics comparison RFM and GFM are in a matrix format at this point (see matrix 4.1). Each field metric from RFM and GFM is taken separately and plotted as a probability density function (PDF). The best performing GFM is determined by statistical testing, as explained in section 4.2.1. The best performing GFM is chosen for SAR simulations. Figure 4.2 shows one example of GFM/RFM comparison for E_{max}/E_{avg}, the details of the simulations are presented in table 4.1, and the statistical testing results are shown on table 4.2.

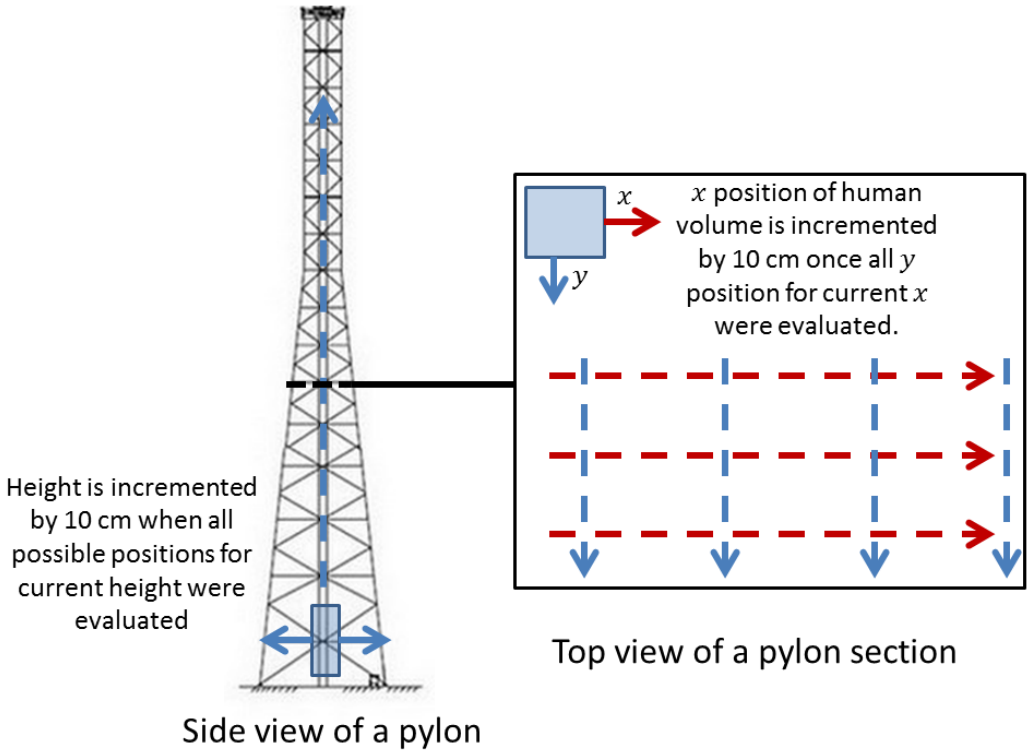

Figure 4.1: On the left, side view on an entire pylon. On the right, top view of pylon section at a specific height.

Inputs	Range [min - max]
Number of dipoles	32
Amplitude	$[0 - 0.5$ A$]$
d_{max}	4 m
d_{min}	0.25 m
Phase	$[0 - 2\pi]$
Orientation θ	$[0 - 2\pi]$
Orientation ϕ	$[0 - 2\pi]$
Iterations	1000000

Table 4.1: Inputs for GFM and RFM shown on figure 4.2.

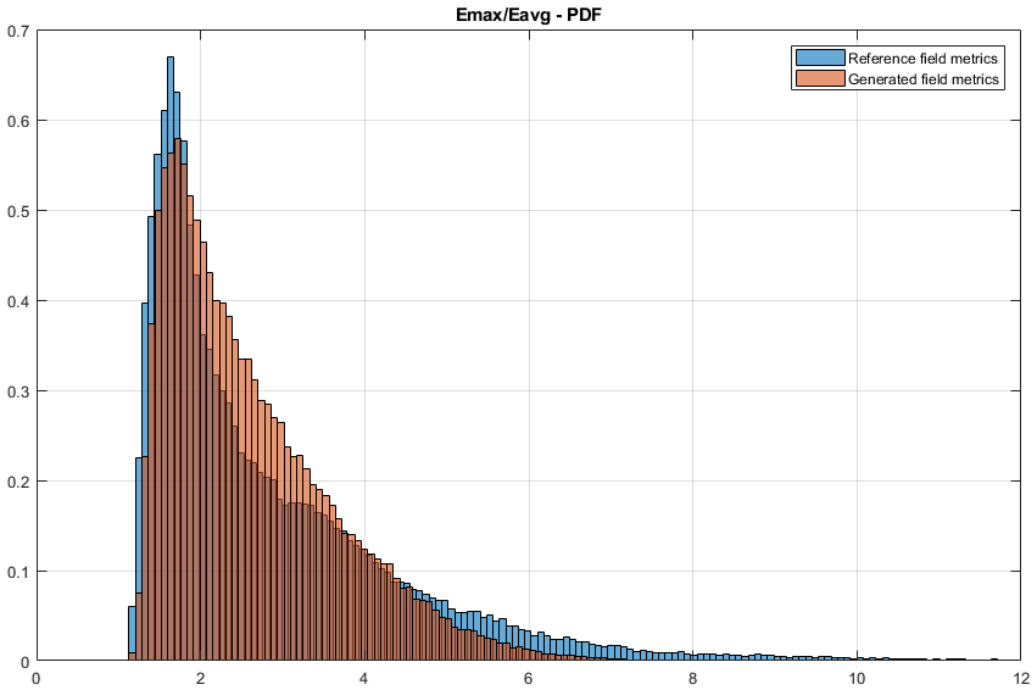

Figure 4.2: E_{max}/E_{avg} comparison for RFM and GFM. Simulation details are presented in table 4.1. Statistical testing is shown on table 4.2.

Statistical test	Result
Histogram intersection	14%
Hellinger distance	80
Jensen-Shannon divergence	2.5

Table 4.2: Statistical tests results of RFM/GFM distributions on figure 4.2.

Phase 3: field metrics collection for SAR simulations Once the best performing GFM is identified in phase 2, a limited number of cases are chosen for SAR simulations. For each chosen case, the GFM are needed in a 1cm resolution, much smaller than the one used for phases 1 and 2. The smaller resolution is needed for 2 reasons: first SAR needs to be correlated to the electric and magnetic field locally for SAR_{10g}. Second, surrogate models need to link SAR results to field metrics, therefore requiring precise results.

Field metrics distributions validation method

As mentioned in section 3.2.2, pylons serve as reference field metrics. Human sized volumes slide inside each pylon, from bottom to top, side to side, thus measuring field metrics in all reachable positions of interest by the worker. For each field metric, a large number of values are obtained and stored as vectors. The same field metrics assessment technique is applied to generated near-fields (section 3.2.1). Therefore, 2 sets of field metrics are obtained. Generated and reference field metrics are represented as probability density functions (PDF) to be compared. Generated field metrics are compared to reference field metrics and saved for SAR assessment when deemed realistic. The comparison consists in statistically testing obtained PDFs. Since generated and reference field metrics (aka GFM and RFM, respectively) are distributions, the validation requires the use of statistical tests [SK+63]. 3 different statistical tests are performed for GFM and RFM.

The first statistical test is the histogram intersection (HI), which measures the shape differences of GFM and RFM histograms, each probed at *nbins*:

$$HI = 1 - \frac{\sum_{j=1}^{nbins} min(H_{GFMj}, H_{RFMj})}{H_{RFMj}} \tag{4.2}$$

H_{GFMj}, H_{RFM} are respectively GFM and RFM histograms.

The second statistical test is the Hellinger distance (HD), which is used to determine the difference between two probability distributions. Given the two probability distributions P_{GFM} and Q_{RFM}, the Hellinger distance is defined as:

$$h(P_{GFM}, Q_{RFM}) = \frac{1}{\sqrt{2}} \left\| \sqrt{P_{GFM}} - \sqrt{Q_{RFM}} \right\|_2 \tag{4.3}$$

The final test is the Jensen-Shannon divergence (JSD), used to measure the behavior of two different distributions. The JSD is based on the Kullback-Leibler divergence (KLD). For two discrete probabilities p_{GFM} and q_{RFM}, the KLD is defined as:

$$D_{KL}(p_{GFM} \,||\, q_{RFM}) = -\sum_{j} p(j) \log \frac{q_{RFM}(j)}{p_{GFM}(j)} \tag{4.4}$$

Let $r = (p_{GFM} + q_{RFM})/2$, then the JSD is expressed as:

$$JSD(p_{GFM}, q_{RFM}) = \frac{D_{KL}(p_{GFM} \,||\, r) + D_{KL}(q_{RFM} \,||\, r)}{2} \tag{4.5}$$

If the HI score is under 5%, GFM and RFM distributions are considered to have the same shape and no further statistical testing is performed. HD is used when histogram intersection does not provide a clear best performer. Last, JSD is used in case both HI and HD fail to show the best performing field metrics. All statistical tests values show better performance with lower results. The GFM with the best performance on all tests provide the best near-field generator inputs, which in turn are used to generate fields for SAR assessment following a design of experiments explained in section 4.2.3.

4.2.2 Field metrics control

Simulations scenarios provide in table 3.9 in section 3.3.5 were performed and then tested. The best performing scenarios are shown on table 4.3. Each scenarios d_{min} and d_{max} are given on table 4.4. GFM7 and 34 perform better respectively in E/H and $c(E)$, while GFM46 performs better at E_{max}/E_{avg} and $(\widehat{E,H})$ field metrics. GFM46's best score in 2 out of 4 field metrics indicates it is the most adapted scenario out of the 4 best scenarios.

4.2.3 Near-field choice for exposure assessment: design of experiments

Millions of near-fields with the appropriate field metrics were generated by phase 3 in section 4.2.1. FDTD simulations for SAR assessment are time consuming and only limited number of near-field exposure cases will be assessed with FDTD. In order to properly reconstruct the SAR distribution with a limited number of simulations, a DoE that sweeps the entire range of

Scenario #		GFM 7	GFM 34	GFM 46	GFM 47
E_{max}/E_{avg}	HI	58%	35%	**5%**	10%
E_{max}/E_{avg}	HD	x	x	x	x
E_{max}/E_{avg}	JSD	x	x	x	x
$(\widehat{E,H})$	HI	8%	7%	**7%**	7%
$(\widehat{E,H})$	HD	50	51	**47**	56
$(\widehat{E,H})$	JSD	x	x	x	x
$c(E)$	HI	11%	**11%**	14%	13%
$c(E)$	HD	84	**73**	90	86
$c(E)$	JSD	x	x	x	x
E/H	HI	**12%**	25%	35%	33%
E/H	HD	**105**	241	291	298
E/H	JSD	x	x	x	x

Table 4.3: GFM performances using histogram intersection (HI), Hellinger Distance (HD) and Jensen-Shannon Divergence (JSD). x indicates the absence of testing necessity. **Bold** values indicate best score per category. Lower is better. Scenarios are referenced in table 4.4.

possible cases is needed.

Since we were able to obtain millions of near-fields, we can assume that our data set has scanned all possible outcomes for the near-field generator. The generated field metrics follow a Gaussian or inverse Gaussian distribution, like seen in figures 3.11 to 3.13. Picking a near-field for SAR assessment using a random uniform draw will cause a discrepancy in the picks, causing highly probable near-fields to appear more in the final group draw, which will cause low-probability cases to be nonexistent. This is detrimental for SAR assessment in our situation, since exposure assessment has to be done with a limited number of SAR simulations. The best SAR assessment in this case would look at all existent possibility with a limited number of simulations. The solution is to perform a Gaussian to Uniform transformation of the field metrics distribution using the Box-Muller transform [Box58], then perform a random uniform group draw for SAR assessment.

In practice, the GFM are not chosen by their index or their actual value, but by their percentiles. This inverse transform does not affect the initial

Scenario	d_{min}	d_{max}
GFM 7	0m	7m
GFM 34	0.15m	4m
GFM 46	0.20m	6m
GFM 47	0.20m	7m

Table 4.4: GFM d_{min} and d_{max} values. This table is a reference for table 4.3.

distribution of GFM. Let X be a continuous random variable with cumulative distribution function F_X, then the random variable $Y = F_X(X)$ has a uniform distribution on $[0, 1]$. The inverse probability integral transform $F_X^{-1}(Y)$ has the same distribution as X.

Let n_i be the i-th SAR simulation, and let $n_{max} = 500$ be the maximum number of SAR simulations that can be performed for this project. n_i can be chosen as a percentile from $U \sim Unif[0, 1]$, then used with the associated CDF F_X to find the correct GFM case.

Using the above mentioned technique, 500 GFM were chosen for SAR simulations.

4.3 Human exposure computation material

4.3.1 Human model, FDTD and homogenization

Human model

The Duke phantom from the Virtual Family (figure 2.2) was used for the specific absorption rate (SAR) computations. The Duke human model was reconstructed by the IT'IS foundation using detailed anatomical information from MRI images [CKH+09]. Tissues conductivities were assigned using the IT'IS database [HNG+12].

FDTD

Due to the different tissues that constitute the human body, 3D phantom models are heterogeneous by nature and are large problems from a computational point of view. The Finite differences in time domain (FDTD) is a

technique used to solve Maxwell's equations that does not require the use of matrix inversion, which is the most computationally costly process. FDTD is intensively used in bioelectromagnetics because of the simplicity of the FDTD method and the absence of matrix inversion.

The electric and magnetic fields used in the ICNIRP and IEEE reference levels (section 2.1.2) are dictated by Maxwell's equations (see equations 4.6). In a media with permittivity ϵ, permeability μ, and conductivity σ, the electromagnetic fields E and H induced by electric and magnetic currents J_i and M_i in time domain can be written as:

$$\begin{aligned} \vec{\nabla} \times \vec{E} &= -\vec{M}_i - j\omega\mu\vec{H} \\ \vec{\nabla} \times \vec{H} &= \vec{J}_i + \sigma\vec{E} + j\omega\epsilon\vec{E} \end{aligned} \tag{4.6}$$

where E (V/m) and H (A/m) are respectively the complex spatial form of electric and magnetic fields, J_i (A/m^2) and M_i (V/m^2) are the electric and magnetic currents supplied to the source, and ∇ is the "Nabla" operator.

The FDTD technique is based on the sampling of the electric and magnetic field vectors $\overrightarrow{E}(x, y, z, t)$ and $\overrightarrow{H}(x, y, z, t)$ over a time and space grid. Finite differences in time domain (FDTD) were used to solve Maxwell's equations to find electric and magnetic fields using the Yee scheme [Yee66] (see figure 4.3). The components of the E and H are sampled at different times and locations, which is done in a leap frog manner (see figure 4.3).

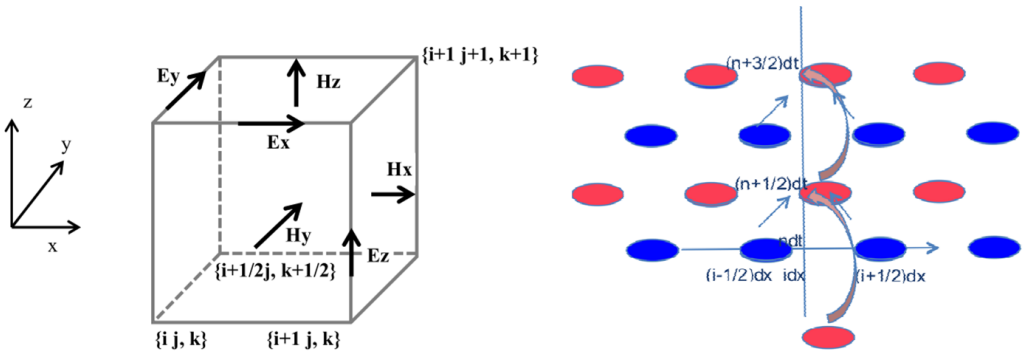

Figure 4.3: Yee scheme (left), leap frog scheme (right).

For FDTD to be stable, the Courant, Friedrichs, and Lewy relationship [CFL67] must be valid:

$$dt \leq \frac{1}{v\sqrt{1/dx^2 + 1/dy^2 + 1/dz^2}} \tag{4.7}$$

where dt, dx, dy, dz are the time and spatial steps, and v is the light velocity in the media. FDTD simulation time depends on the grid size of the 3D space and the frequency. FDTD simulation time is higher when the frequency and the grid size of the 3D space are lower. Considering that SAR simulations need a 2-mm resolution at the most to have precise results, and considering the FM frequency band ($88 - 108$ MHz in Europe), FDTD simulations could last to an estimated 192h (8 days). Fortunately, the Tissues Homogenization Technique can be used to significantly reduce computation time.

Homogenization

The 2-mm Duke model was rescaled to 4-mm using a tissue homogenization technique (THT) [Wia16] [PLL+06], which reduces the computational cost while providing an acceptable accuracy of SAR assessment. The tissues of the human body are defined in fine grid so that the dielectric properties can be found in coarse grid. The dielectric properties are then used with FDTD to find the electric field in the coarse grid. E field values are interpolated in the fine grid so that SAR can be calculated. In our trials, THT showed an 8% error in electric field strength when applied at 100MHz. Computation time was reduced from an estimated 192h (8 days) to 12 hours for one single SAR assessment using THT. Figure 4.4 shows an overview of the tissue homogenization technique.

4.3.2 Near-field to SAR via equivalent principle

In the case of a source far from the object under analysis, it is computationally costly to model the source and the person together and compute this configuration with FDTD. In such a case, the equivalent principle [RRS00] can be used to take into account the electric and magnetic fields emitted by the antenna without modeling the source nor the space between the antenna and the human model. The assessment of the fields induced in a given volume by a source outside of the volume can be done using equivalent currents located on the surface of the volume (see figure 4.5). The equivalent principle

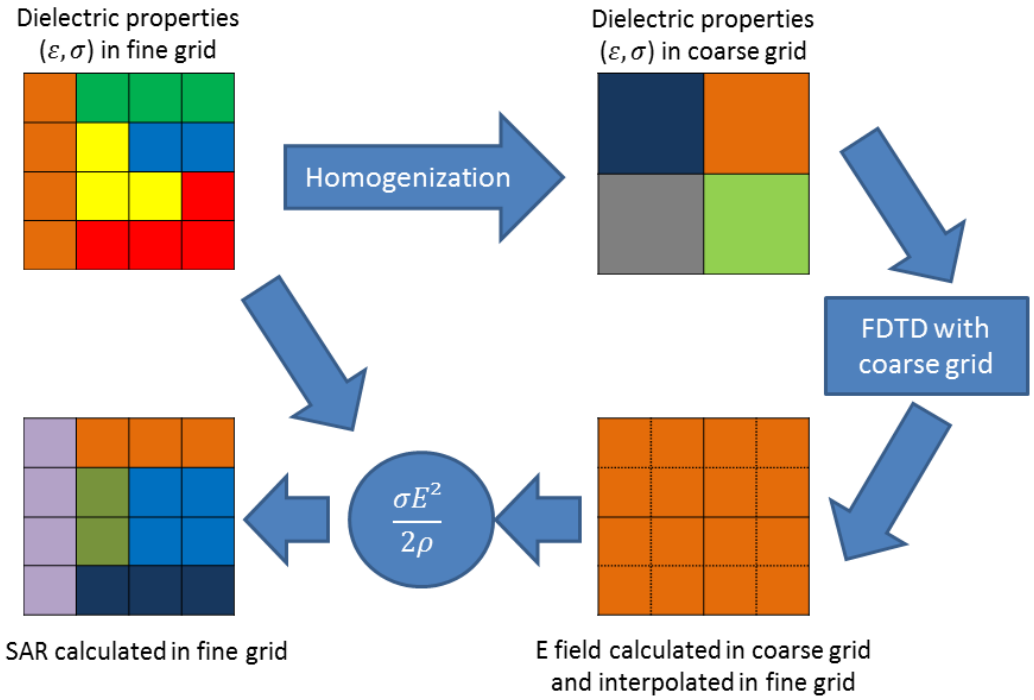

Figure 4.4: Tissue homogenization technique applied to SAR assessment.

is used to compute SAR induced by EMF in a human sized volume via the Duke human model and the FDTD method. Such an equivalent principle is implemented via a "Huygens box". The near-field generator was adjusted to work with a FDTD computation machine. The generator is used to compute the Huygens box, and from then proceed to do an FDTD calculation.

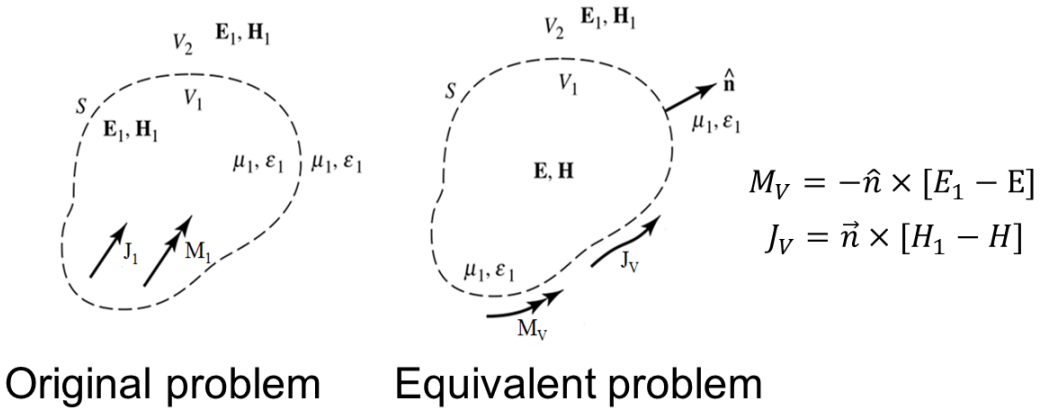

Figure 4.5: Equivalent principle, original problem on the left, equivalent problem on the right.

4.4 Conclusion

The near-field exposure assessment methodology validation is performed using field metrics which were validated and controlled in this chapter. The generated field metrics scenarios provided in chapter 3 were tested and one was selected for SAR simulations. The design of experiments for FDTD simulations was given. Last, the human exposure computation material was explained. The next chapter will show and discuss results, and provide SAR surrogate models for near-field exposure.

Chapter 5

Results, surrogate models and discussion

5.1 Introduction

The near-field assessment methodology was validated in the previous chapter. In this chapter, the SAR results are shown and the uncertainty quantified. Surrogate models are proposed with their numerical validation for both local and whole-body SAR. Finally, results and surrogate models are discussed last.

5.2 SAR Results

5.2.1 Local and whole-body SAR results

Five hundred FDTD simulations were performed using the near-field assessment methodology. In order to compare local SAR results, all results were normalized to different averaged field strengths (E_{avg}) from 30 V/m to 100 V/m. We define local SAR ratio R_{10g} as

$$R_{10g} = \frac{SAR_{10g}}{SAR_{10g}\ limit} \tag{5.1}$$

where SAR_{10g} is the peak local SAR and SAR_{10g} *limit* is 10 W/kg or 20 W/kg [ICN20], depending on the SAR_{10g} position. $R_{10g} > 1$ indicates non compliance, which is represented by the right side of the vertical line in figure 5.1. Global exposure impact on local exposure can be better observed when R_{10g} is analyzed for different E_{avg} values. R_{10g} was calculated for different E_{avg} values then arranged in cumulative distributions functions (CDF) as shown in figure 5.1. The vertical line shows the rate at which $R_{10g} < 1$, which means local SAR compliance rate. Based on the limited number simulations that were performed, 81% of local exposure cases are compliant ($R_{10g} < 1$) when $E_{avg} = 61$ V/m. The compliance rate is respectively 34%, 58% and 98% when $E_{avg} = 100$ V/m, 80 V/m and 30 V/m. Figure 5.1 shows R_{10g} does not depend on E_{max} solely, as global exposure levels represented by whole-body SAR (WBSAR) and E_{avg} in the human sized volume seems to have a major impact on compliance rates. WBSAR represents global exposure, which is best described by E_{avg}. Figure 5.2 shows the empirical CDFs of R_{wb} depending on E_{avg}. R_{wb} is defined as

$$R_{wb} = \frac{WBSAR}{WBSAR_{limit}} \tag{5.2}$$

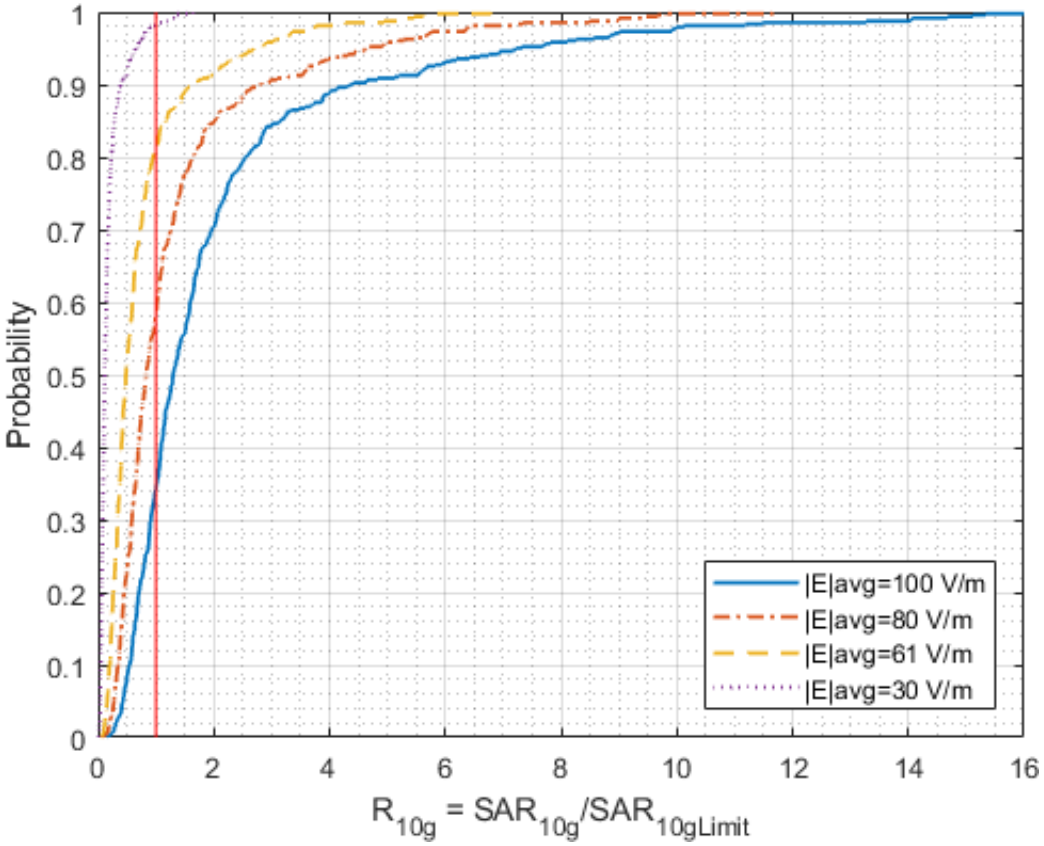

Figure 5.1: Empirical cumulative distribution function of R. All results were normalized to E_{avg} from 30 V/m to 100 V/m.

where $WBSAR_{limit}$ is 0.4 W/kg [ICN20]. $R_{wb} \leq 1$ is defined as compliant WBSAR cases. R_{wb} CDF is computed for different E_{avg} values in figure 5.2. WBSAR compliance rate is 99.6% when $E_{avg} = 100$ V/m. When $E_{avg} \leq 80$ V/m, all simulated WBSAR cases are shown to be compliant.

All $R_{10g} < 1$ and $R_{wb} < 1$ are summarized in table 5.1.

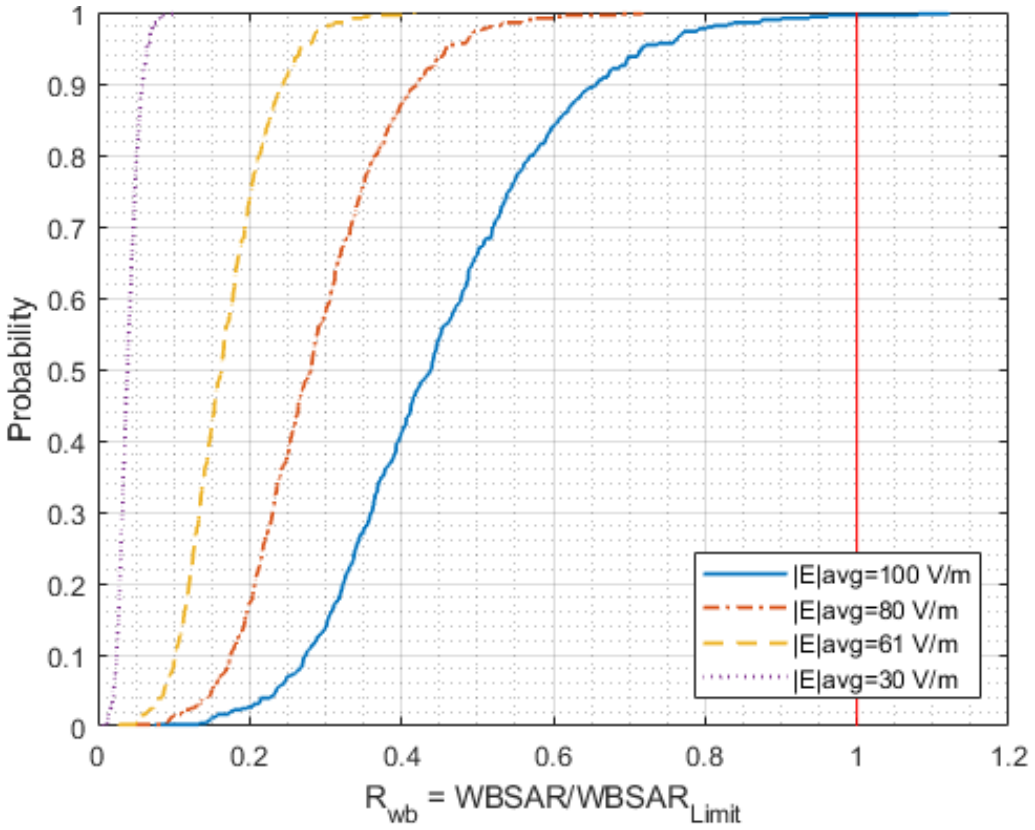

Figure 5.2: R_{wb} CDFs for different E_{avg} values.

E_{avg}	$R_{10g} < 1$ compliance rate	$R_{wb} < 1$ compliance rate
100 V/m	34%	99.6%
80 V/m	58%	100%
61 V/m	81%	100%
30 V/m	98%	100%

Table 5.1: $R_{10g} < 1$ and $R_{wb} < 1$ compliance rates for different E_{avg} values based on 500 SAR simulations. Table entries were extracted from figures 5.1 and 5.2.

5.2.2 Uncertainty quantification and confidence intervals for SAR results

Introduction

Figures 5.1 and 5.2 were obtained with 500 SAR simulations, which means the cumulative distribution functions and the specified compliance rates could change if more SAR simulations were performed. Hence the uncertainty on compliance rates has to be quantified and confidence intervals must be determined without knowing the final distribution shape. We used the bootstrapping method based on resampling [ET86, MMDS03] to find the confidence intervals for the compliance rates.

Method

The bootstrapping method procedure is as follows:

- Resample the available data by creating hundreds of new samples with replacement from the original sample, which means the R_{10g} or R_{wb} points are duplicated in such a design that the same point can reappear in more than one observation.
- Find the bootstrap distribution by performing millions of draws of 500 points out of the resampled data.
- Use the boostrap distribution to find the confidence interval.

The bootstrapping method was applied to the 500 R_{10g} and R_{wb} results to find the confidence intervals for both. The bootstrap distribution can be seen on figures 5.3 and 5.4, results were extracted on table 5.2.

Results

Four thousand resamples of the original 500 samples were performed, so that in total the available pool of points has 2 millions of observations. The compliance rate is calculated for both SAR_{10g} and WBSAR. We find the R_{10g} and R_{wb} bootstrapping histograms from which we can derive the confidence intervals for SAR_{10g} and WBSAR results for $E_{avg} = 100$ V/m, which are shown on table 5.2. The uncertainty quantification shows confidence intervals at different confidence levels. Confidence levels shown in table 5.2 correspond

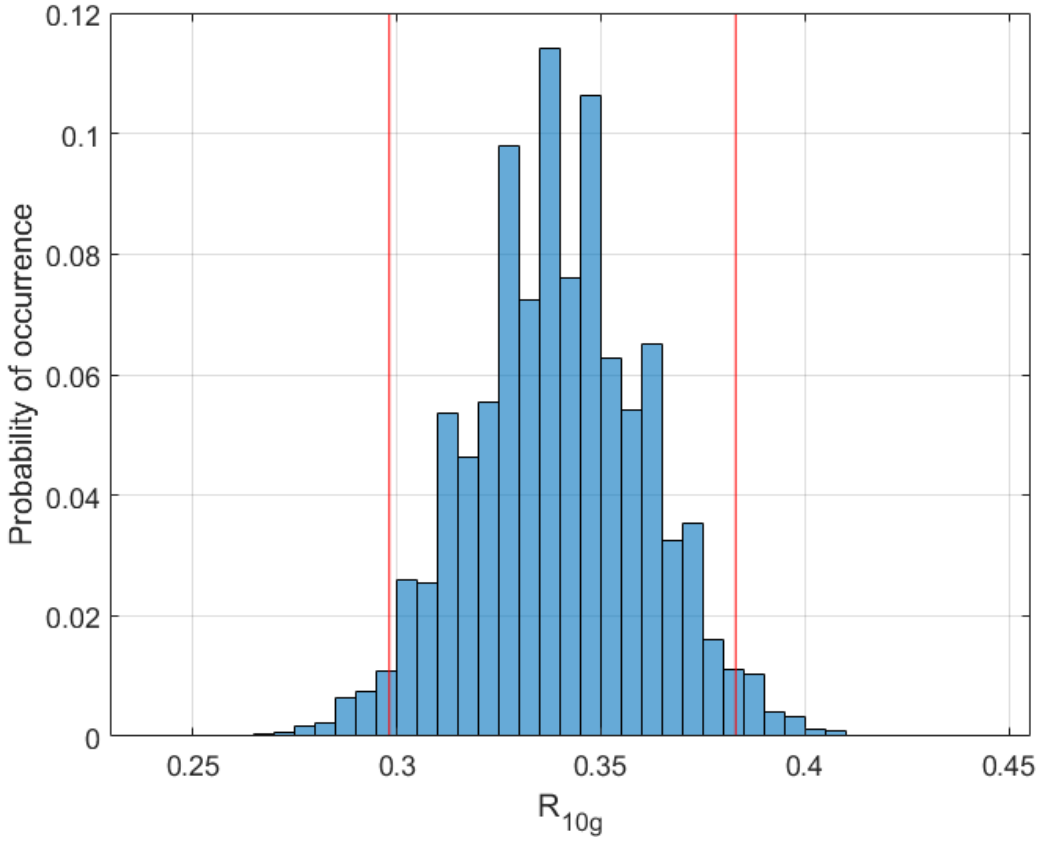

Figure 5.3: Bootstrap distribution for R_{10g}. Vertical lines indicate confidence interval at 95% certainty.

respectively to one to three standard deviations on the bootstrap histogram. Statistical testing using histogram intersection and Hellinger distance showed that the obtained bootstrapping histogram is a normal distribution with parameters $(\mu = 0.34, \sigma = 0.02)$ for R_{10g} and $(\mu = 1.00, \sigma = 0.003)$ for R_{wb}. The confidence intervals on table 5.2 show that results in figures 5.1 and 5.2 could lead to different R_{10g} and R_{wb} values included in the intervals, had we performed more SAR simulations. The 500 observations were sufficient to give a rough estimate of compliance ratios with an uncertainty span of 10% for R_{10g} and less than 2% for R_{wb}, which shows that the former may need more FDTD simulations to reduce uncertainty whereas the latter is correctly estimated with 500 observations. This phenomenon is explained by the fact that R_{10g} is more variable than R_{wb}.

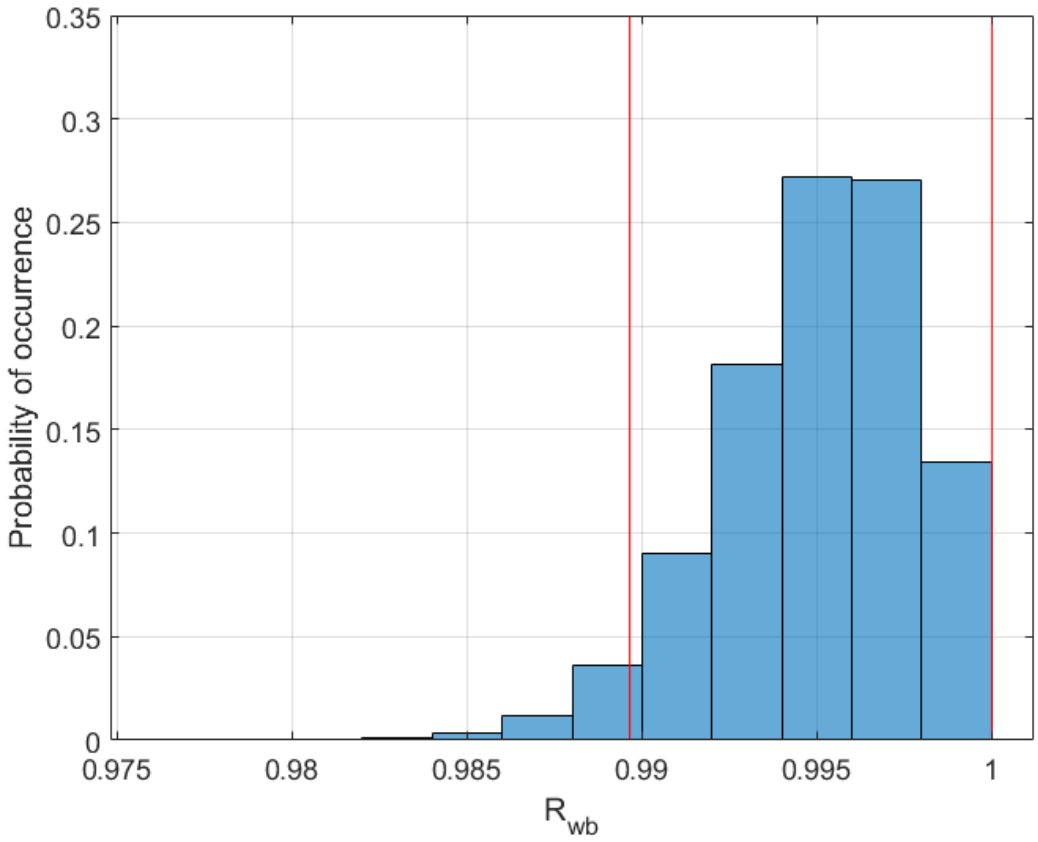

Figure 5.4: Bootstrap distribution for R_{wb}. Vertical lines indicate confidence interval at 95% certainty.

R_{10g} confidence intervals			
Confidence level	68%	95%	99%
$E_{avg} = 100$ V/m	$32.9 - 35.0\%$	$29.8 - 38.3\%$	$28.6 - 39.5\%$
R_{wb} confidence intervals			
Confidence level	68%	95%	99%
$E_{avg} = 100$ V/m	$99.4 - 99.8\%$	$98.9 - 100\%$	$98.8 - 100\%$

Table 5.2: R_{10g} and R_{wb} confidence intervals, extracted from figures 5.3 and 5.4.

5.3 Local and whole-body SAR regression surrogate models

5.3.1 Methodology

Figure 5.2 suggests high correlation between WBSAR and E_{avg}. Based on figure 5.1, it is suspected SAR_{10g} depends on local exposure associated with E_{max}, and also on global exposure associated with E_{avg}. Global exposure acts as a baseline for local exposure (figure 5.1), as it sets a minimum local exposure level which can only be increased by E_{max}. Therefore, surrogate models for local exposure will most likely relate SAR_{10g} to both E_{max} and E_{avg}, whereas the surrogate model for global exposure will link $WBSAR$ to E_{avg}.

Since SAR and the Poynting vector (which represents the power transfer per unit area) are proportional to E^2, the squared electric field will be considered as input of the surrogate modeling. Both maximum SAR_{10g} and WBSAR are highly correlated with E field as shown on table 5.3. The high correlation justifies the use of a machine learning modeling technique called linear regression [Bis06] [GBC16].

Linear regression requires a data set that will minimize error and maximize goodness of fit. The 500 SAR simulations will be divided into 2 groups: train and test [HTF09]. The training data set is used to determine the regression coefficients, whereas the test data set is used to calculate the R^2 value, which will determine the goodness of the fit [GSN90] [DS98]:

$$R^2 = 1 - \frac{\sum_{i=1}^{n}(y_i - \hat{y}_i)^2}{\sum_{i=1}^{n}(y_i - \bar{y})^2} \tag{5.3}$$

where n is the number of samples, y_i is the sample i, $\hat{y}_i$ is the predicted value and $\bar{y}$ the average of all samples.

Ten thousand regressions are computed with randomly chosen data points for both test and train groups. The chosen points are different in each simulation, each giving a new R^2 value. The metric allowing discrimination is averaged R^2.

Correlation	E^2_{max}	E^2_{avg}
SAR_{10g}	90.9%	97.5%
$WBSAR$	91.2%	98.6%

Table 5.3: Table of correlations between SAR and electric field.

5.3.2 SAR surrogate models

Local SAR surrogate model

Since SAR_{10g} has different limits based on its peak localization being in the head and trunk or limbs, it is appropriate to find a surrogate model for each. Thus all data is divided into head and trunk or limbs, which are respectively 43% and 57% of all SAR_{10g} localizations. Best R^2 performance shows the most accurate surrogate model is given by 70 and 90 training data points respectively for SAR_{10g} localized in head & trunk and limbs. The SAR_{10g} regression model shows that basic restrictions levels for head & trunk and limbs are exceeded respectively when $E_{max} > 187$ V/m and $E_{max} > 310$ V/m, assuming that $E_{avg} = 61$ V/m in both cases. SAR_{10g} is written

$$SAR_{10g} = \beta_0 \times E^2_{avg} + \beta_1 \times E^2_{max} \tag{5.4}$$

with β coefficients provided in table 5.4. Figure 5.5 shows the regression models and the SAR simulation results.

Coefficients	β_0	β_1
Head & trunk	2.0×10^{-3}	7.3×10^{-5}
Limbs	1.9×10^{-3}	1.3×10^{-4}

Table 5.4: Table of β coefficients for SAR_{10g} surrogate models. Models are shown on figure 5.5.

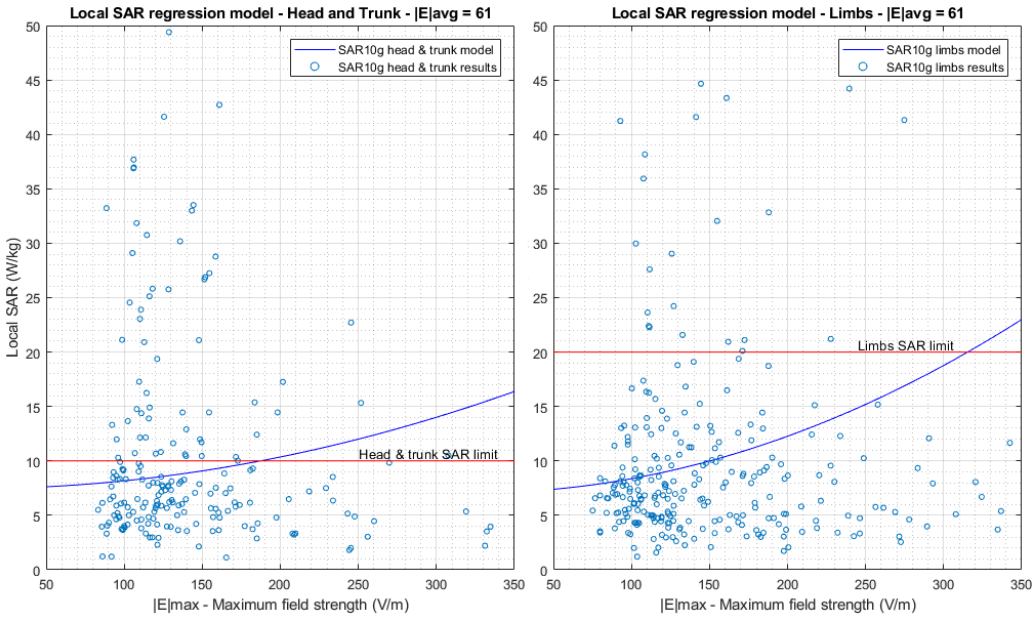

Figure 5.5: Local SAR regression models (solid lines) and local SAR simulation results (circles) versus E_{max}. Head & trunk local SAR on left figure, limbs local SAR on the right figure. Results are shown for $E_{avg} = 61$ V/m.

Whole-body SAR surrogate model

Best R^2 performance shows the most accurate surrogate model for WBSAR is given by 160 training points. The regression model shows that WBSAR limit of $0.4W/kg$ is reached when $E_{avg} > 122$ V/m. WBSAR is described by

$$\begin{aligned} WBSAR &= \beta \times E_{avg}^2 \\ \beta &= 2.7 \times 10^{-5}. \end{aligned} \tag{5.5}$$

WBSAR surrogate model shows a higher reference value than actual simulations in figure 5.2 where it was shown that $E_{avg} = 100$ V/m causes a non-compliance rate of 1%. Figure 5.6 shows the whole-body SAR regression model and the simulation results.

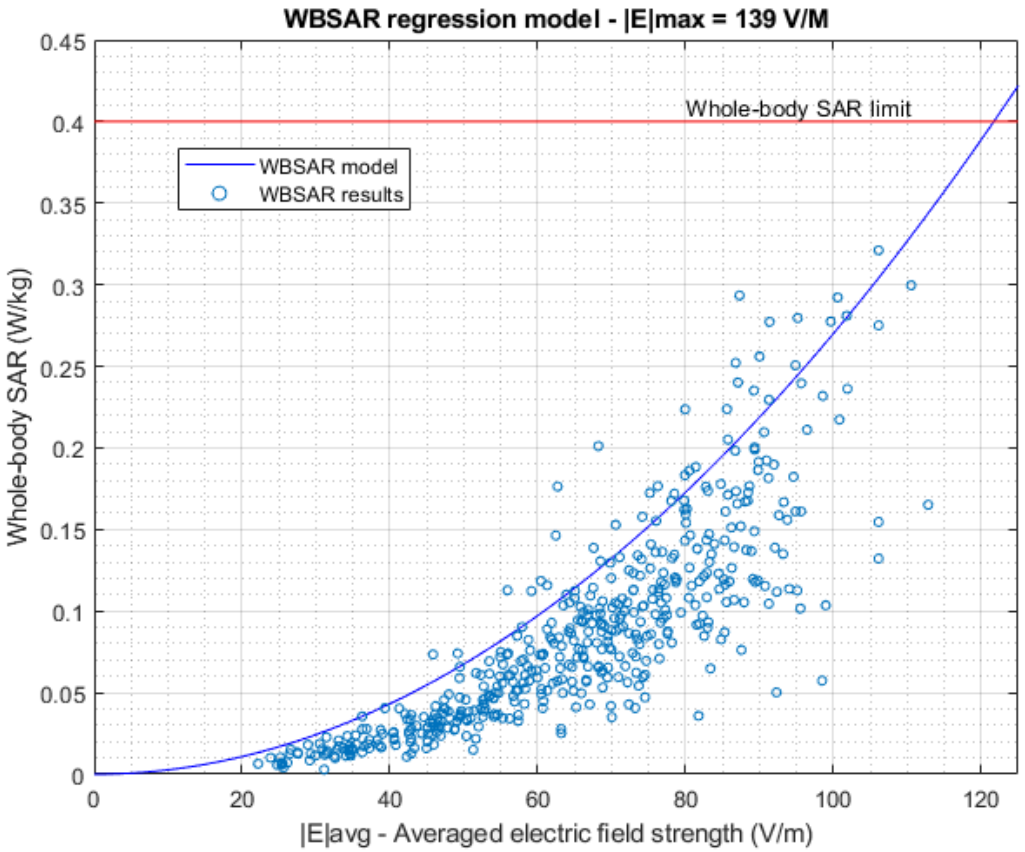

Figure 5.6: Whole-body SAR regression model (solid line) and whole-body SAR simulation results (circles) versus E_{avg}. Results are shown for E_{max} = 139 V/m.

5.3.3 Numerical validation of surrogate models

Since SAR in the human body is impossible to measure, the results of WBSAR and SAR_{10g} from the estimation formulas were validated by comparison to the numerical FDTD results shown in section 5.2.1. The histograms of the deviation of the estimation formulas from the numerical FDTD simulations are presented in figures 5.7 to 5.9. The WBSAR and SAR_{10g} results are displayed as a ratio to the SAR limit such as:

$$Deviation(dB) = 10 \times \log_{10}(\frac{SAR_{model}}{SAR_{sim}}) \tag{5.6}$$

where SAR_{model} is the WBSAR or SAR_{10g} value obtained using the estimation formulas, SAR_{sim} is the WBSAR or SAR_{10g} value obtained through FDTD simulations. In figures 5.7 to 5.9, positive deviations mean that SAR_{model} is conservative when compared to numerical FDTD simulations SAR_{sim}, whereas negative deviations mean that estimation formulas are not conservative. It can be observed in figures 5.7 to 5.9 that estimation formulas are not conservative in all cases. Based on 500 SAR assessments using the methodology described in this paper, estimation formulas are conservative in 91%, 63%, and 70% of cases respectively for WBSAR, head & trunk SAR_{10g}, and limbs SAR_{10g} models. Since the conservativeness of estimation formulas was not an objective in this work, it is no surprise that conservative percentages are under 100%. Other papers built surrogate models [GVK+11] using a 95-th percentile cuboid [HKWF07] [HIF+08], which is a human body leading to a conservative exposure for 95% of the population. Figures 5.7 to 5.9 also show the difference between surrogate models and actual SAR observations for the same inputs.

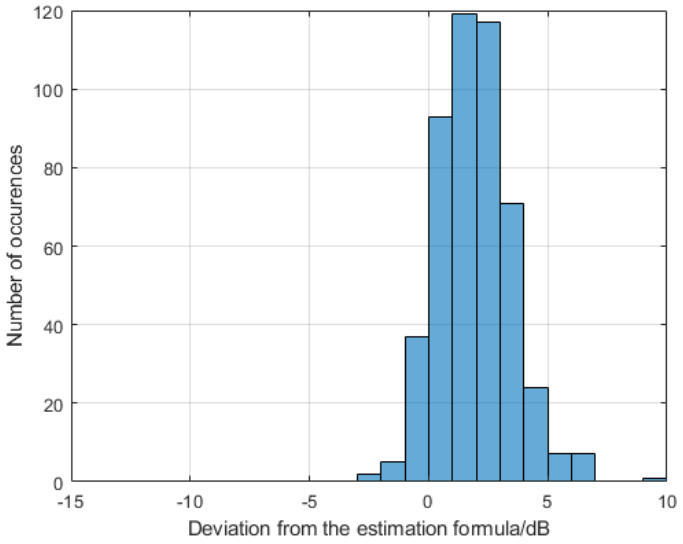

Figure 5.7: Histograms of the deviation between WBSAR simulation results and estimation formula.

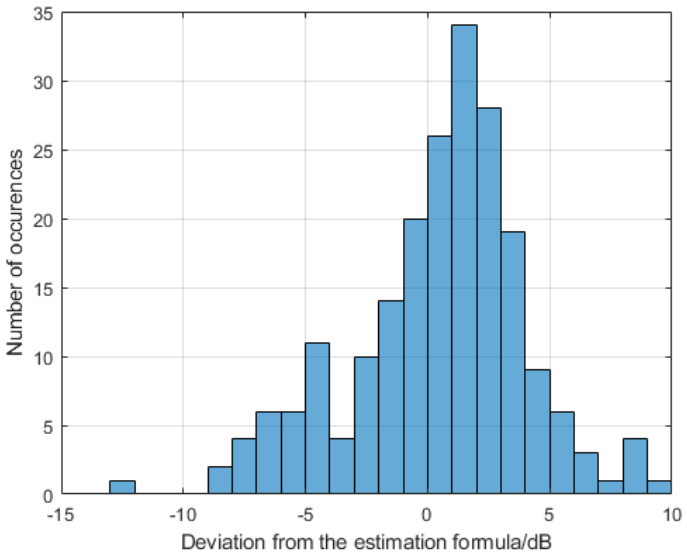

Figure 5.8: Histograms of the deviation between head & trunk SAR_{10g} simulation results and estimation formula.

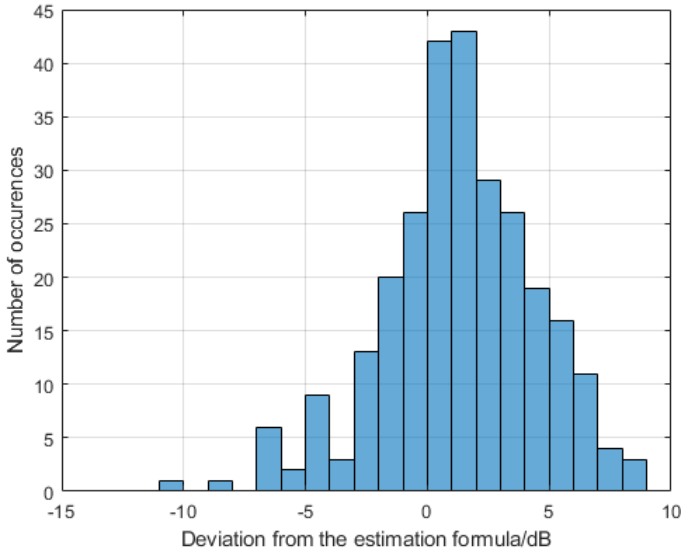

Figure 5.9: Histograms of the deviation between limbs SAR_{10g} simulation results and estimation formula.

5.3.4 Discussion

Surrogate models accuracy and frequency dependence

Although the local SAR and WBSAR surrogate models were obtained using FDTD simulations at 100MHz, they are valid for all FM frequencies with a maximum error of 5%. In fact, SAR is frequency dependent due to the human tissues conductivities being frequency dependent, which can change by 5% at the most in the FM frequency range. To ensure their precision, the surrogate models were built using E_{avg} sampled at a 1cm step. However they can be used with E_{avg} sampled at other grid steps, as reference **??** showed that electric field averaging using a limited number of points is valid with an error.

Surrogate models limitations

The surrogate models presented in this paper were found using linear regression, a statistical method for examining the relationship between a dependent output and one or more independent inputs. Hence, the accuracy of the obtained surrogate models depends on the number of SAR simulations. The linear regression models were trained so as to avoid over-fitting. But linear regression remains sensitive to outliers, which can cause models to hide the relationship between variables. Other methods such as Polynomial Chaos Expansion and Kriging were looked at when performing the study. Due to different maximum field strengths causing same peak local SAR values, both surrogate modeling methods could not be used.

Uncertainty on results

In order to bypass limitations imposed by the size of the FDTD computations in FM frequencies, the human model was homogenized with an 8% error on the electric field strength results and a 16% error on local and whole-body SAR results. The uncertainty quantification using bootstrapping methods exposed the confidence intervals at different confidence level. The local and whole-body surrogate models in this paper are approximations with their deviation from reality studied and presented in figures 5.7 to 5.9. It is important to be aware that any conclusion led to by the results in this paper must take into account all uncertainties, and that the surrogate models for local and whole-body SAR are mere approximations.

5.4 Conclusion

This work presented a new method for exposure assessment in near-field environments by focusing on the electric and magnetic fields rather than sources. This method depends on a chain in which there is a near-field generation and characterization, statistical testing for near-field validation, local and whole-body SAR simulations via FDTD and finally exposure assessment substitute formulas using linear regression. An application in near-field FM exposure was presented, using 500 local and whole-body SAR simulations, but the methodology could have been applied for different frequencies and sources.

Due to local SAR simulations showing a dependency to both maximum and averaged field strength in a human sized volume, local SAR estimation formulas are provided with these two quantities. The whole-body SAR estimation formula only uses the averaged electric field strength in a human sized volume. Both SAR quantities were linked to electric fields that can be measured on site using a field-meter.

Chapter 6

General Conclusion

The main objectives of this PhD thesis were to assess EMF exposure in near-field environments found in pylons and find basic restrictions estimation formulas using reference levels. In this respect, a near-field exposure assessment methodology was proposed and validated. SAR simulations were conducted and SAR estimations formulas were provided.

The literature on near-field exposure assessment was reviewed, and the different definitions of near-field in different standards were presented in chapter 2. After the literature review, it was shown that a worst case scenario approach in which SAR is studied where electric field is the highest is often the privileged methodology. The different exposure configurations in the literature and the near-field definitions in standards showed the need for a generalized exposure assessment methodology.

The near-field exposure methodology based on the study of field metrics was presented in chapter 3. Numerical simulations and calculations of real and generic pylons validated by a broadcasting operator provided a near-field reference. Random near-fields were generated using a combination of dipoles. The near-field generation fitting was explained using sensitivity analysis, and a design of experiments with the near-field generator was presented.

The near-field exposure methodology was presented in chapter 4. The field metrics collection, analysis, and control were performed, which lead to the selection of the near-field generator inputs. A design of experiments for SAR simulations was presented. The human exposure computation material including the human model, FDTD, homogenization technique, and the equivalent principle were presented in chapter 4.

Local & whole-body SAR results and estimation formulas were presented in chapter 5. Five hundred SAR simulation results were presented and their relation to electric field was analyzed. The uncertainty of the simulation results was studied and quantified. The estimation formulas were found using a machine learning technique called linear regression. The deviation of the estimation formulas from simulation results was quantified.

This work presented a chain of methods and techniques assembled together to go from reference simulations of transmission pylon to find exposure values and surrogate models. The near-field characterization method is the novelty

of this work. This method is based on field metrics rather than electric field or exposure values, with errors and deviations from reality. The near-field generator presented in chapter 3 remains a mathematical construction, with limitations found in the very near-field. The near-field generator configuration presented in chapter 4 is a solution among others, that was chosen because of statistical performances of electric field ratio and angles between electromagnetic fields. The configuration proved to be less performant in the other two field metrics.

The exposure results were found using FDTD simulations. As explained previously, there are a number of errors that have to be kept in mind. To reduce SAR simulation time, a human model was created using a tissues homogenization technique, which came with an 8% error on electric field. The uncertainty on the SAR results was quantified and presented. Later, the surrogate models presented in chapter 5 were found using the 500 SAR simulations results. The deviation of the surrogate models from the SAR simulations was presented. Last but not least, another 5% error was found when using the surrogate models for FM frequencies other than 100 MHz.

This work presented an application in FM frequencies, specifically 100 MHz. It can be expanded by applying the near-field assessment methodology to different frequencies, and building SAR surrogate models for each frequency. In regards to SAR assessments done in chapter 5, future works should include using the near-field exposure method with a 95-th percentile cuboid technique to find estimation formulas leading to a conservative exposure. The surrogate models presented in chapter 5 were built using linear regression, a simple technique that is often used in machine learning. While being easy to implement and very efficient to train, linear regression has some disadvantages. Linear regression can be overfitting when there are more features than observations, this problem was avoided by doing enough simulations. Linear regression is sensitive to outliers, therefore a training method that emphasizes a random selection of points in each iteration was used. Instead of linear regression, future works can study the use of other more developed machine learning techniques such as neural networks.

Bibliography

[Bal16] Constantine A Balanis. *Antenna theory: analysis and design*. John wiley & sons, 2016.

[Ban99] Rajeev Bansal. The far-field: How far is far enough? *Applied Microwave & Wireless*, 11(11):59–60, 1999.

[Bil14] Nasir Bilal. Implementation of sobol's method of global sensitivity analysis to a compressor simulation model. 2014.

[Bis06] Christopher M Bishop. *Pattern recognition and machine learning*. springer, 2006.

[Box58] George EP Box. A note on the generation of random normal deviates. *Ann. Math. Stat.*, 29:610–611, 1958.

[BP16] Emanuele Borgonovo and Elmar Plischke. Sensitivity analysis: a review of recent advances. *European Journal of Operational Research*, 248(3):869–887, 2016.

[C+18] Federal Communications Commission et al. Body tissue dielectric parameters, 2018.

[CFL67] Richard Courant, Kurt Friedrichs, and Hans Lewy. On the partial difference equations of mathematical physics. *IBM journal of Research and Development*, 11(2):215–234, 1967.

[CHG+10] Emmanuelle Conil, Abdelhamid Hadjem, Azeddine Gati, Man-Fai Wong, and Joe Wiart. Influence of plane-wave incidence angle on whole body and local exposure at 2100 MHz. *IEEE Transactions on Electromagnetic Compatibility*, 53(1):48–52, 2010.

[CHL+08] E Conil, A Hadjem, F Lacroux, MF Wong, and J Wiart. Variability analysis of SAR from 20 MHz to 2.4 GHz for different adult and child models using finite-difference time-domain. *Physics in Medicine & Biology*, 53(6):1511, 2008.

[CKH+09] Andreas Christ, Wolfgang Kainz, Eckhart G Hahn, Katharina Honegger, Marcel Zefferer, Esra Neufeld, Wolfgang Rascher, Rolf Janka, Werner Bautz, Ji Chen, et al. The Virtual Family—development of surface-based anatomical models of two adults and two children for dosimetric simulations. *Physics in Medicine & Biology*, 55(2):N23, 2009.

[DS98] Norman R Draper and Harry Smith. *Applied regression analysis*, volume 326. John Wiley & Sons, 1998.

[ET86] Bradley Efron and Robert Tibshirani. Bootstrap methods for standard errors, confidence intervals, and other measures of statistical accuracy. *Statistical science*, pages 54–75, 1986.

[Eur13] European Parliament. Directive 2013/35/EU of the European Parliament and of the council of 26 june 2013 on the minimum health and safety requirements regarding the exposure of workers to the risks arising from physical agents. *Official Journal of the European Union L*, 179, 2013.

[Eur14] European Parliament. Directive 2014/53/EU of the European Parliament and of the Council of 16 April 2014 on the harmonisation of the laws of the Member States relating to the making available on the market of radio equipment. *Official Journal of the European Union L*, 153, 2014.

[FD05] RP Findlay and PJ Dimbylow. Effects of posture on FDTD calculations of specific absorption rate in a voxel model of the human body. *Physics in Medicine & Biology*, 50(16):3825, 2005.

[FD09] RP Findlay and PJ Dimbylow. Spatial averaging of fields from half-wave dipole antennas and corresponding SAR calculations in the NORMAN human voxel model between 65 MHz and 2 GHz. *Physics in Medicine & Biology*, 54(8):2437, 2009.

[GBC16] Ian Goodfellow, Yoshua Bengio, and Aaron Courville. *Deep learning*. MIT press, 2016.

[Goo05] Joseph W Goodman. *Introduction to Fourier optics*. Roberts and Company Publishers, 2005.

[GSN90] Stanton A Glantz, Bryan K Slinker, and Torsten B Neilands. *Primer of applied regression and analysis of variance*, volume 309. McGraw-Hill New York, 1990.

[Gui98] Guideline, ICNIRP. Guidelines for limiting exposure to time-varying electric, magnetic, and electromagnetic fields (up to 300 GHz). *Health phys*, 74(4):494–522, 1998.

[GVK+11] Marie-Christine Gosselin, Günter Vermeeren, Sven Kuhn, Valpré Kellerman, Stefan Benkler, Tero MI Uusitupa, Wout Joseph, Azeddine Gati, Joe Wiart, Frans JC Meyer, et al. Estimation formulas for the specific absorption rate in humans exposed to base-station antennas. *IEEE transactions on electromagnetic compatibility*, 53(4):909–922, 2011.

[HIF+08] Akimasa Hirata, Naoki Ito, Osamu Fujiwara, Tomoaki Nagaoka, and Soichi Watanabe. Conservative estimation of whole-body-averaged SARs in infants with a homogeneous and simple-shaped phantom in the GHz region. *Physics in Medicine & Biology*, 53(24):7215, 2008.

[HJ88] Jørgen Hald and Frank Jensen. *Spherical near-field antenna measurements*, volume 26. Iet, 1988.

[HKWF07] Akimasa Hirata, Sachiko Kodera, Jianqing Wang, and Osamu Fujiwara. Dominant factors influencing whole-body average SAR due to far-field exposure in whole-body resonance frequency and GHz regions. *Bioelectromagnetics: Journal of the Bioelectromagnetics Society, The Society for Physical Regulation in Biology and Medicine, The European Bioelectromagnetics Association*, 28(6):484–487, 2007.

[HLD+05] Abdelhamid Hadjem, David Lautru, Christian Dale, Man Faï Wong, Victor Fouad Hanna, and Joe Wiart. Study of specific

absorption rate (SAR) induced in two child head models and in adult heads using mobile phones. *IEEE Transactions on Microwave Theory and Techniques*, 53(1):4–11, 2005.

[HNG+12] PA Hasgall, E Neufeld, MC Gosselin, A Klingenböck, N Kuster, P Hasgall, and M Gosselin. IT'IS Database for thermal and electromagnetic parameters of biological tissues. 2012.

[HTF09] Trevor Hastie, Robert Tibshirani, and Jerome Friedman. *The elements of statistical learning: data mining, inference, and prediction*. Springer Science & Business Media, 2009.

[ICN20] ICNIRP. Guidelines for Limiting Exposure to Electromagnetic Fields (100 kHz to 300 GHz). *Health Physics*, 2020.

[IEE10] IEEE Standards Coordinating Committee 39. IEEE standard for safety levels with respect to human exposure to radio frequency electromagnetic fields, 3kHz to 300GHz. *IEEE C95.1-2010*, 2010.

[IEE19] IEEE Standards Coordinating Committee 39. IEEE standard for safety levels with respect to human exposure to radio frequency electromagnetic fields, 3kHz to 300GHz. *IEEE C95.1-2019*, 2019.

[IM93] Sobol' IM. Sensitivity estimates for nonlinear mathematical models. *Math. Model. Comput. Exp*, 1(4):407–414, 1993.

[KCH+11a] T Kientega, E Conil, A Hadjem, A Gati, E Richalot, M-F Wong, O Picon, and J Wiart. A new approach to assess the Specific Absorption Rate induced by multiple plane waves at 2.1 GHz. In *Proceedings of the 5th European Conference on Antennas and Propagation (EUCAP)*, pages 2589–2592. IEEE, 2011.

[KCH+11b] Thierry Kientega, Emmanuelle Conil, Abdelhamid Hadjem, Elodie Richalot, Azzedine Gati, Man Fai Wong, Odile Picon, and Joe Wiart. A surrogate model to assess the whole body SAR induced by multiple plane waves at 2.4 GHz. *annals of telecommunications-annales des télécommunications*, 66(7-8):419–428, 2011.

[KHS+16] Anis Krayni, Abdelhamid Hadjem, Alain Sibille, Christophe Roblin, and Joe Wiart. A novel methodology to evaluate uplink exposure by personal devices in wireless networks. *IEEE Transactions on Electromagnetic Compatibility*, 58(3):896–906, 2016.

[KHV+17] Anis Krayni, Abdelhamid Hadjem, Günter Vermeeren, Alain Sibille, Christophe Roblin, Wout Joseph, Luc Martens, and Joe Wiart. Modeling and characterization of the uplink and downlink exposure in wireless networks. *International Journal of Antennas and Propagation*, 2017, 2017.

[LC04] S Laybros and PF Combes. On radiating-zone boundaries of short, $\lambda/2$, and λ dipoles. *IEEE antennas and propagation magazine*, 46(5):53–64, 2004.

[LPH+19] Ae-Kyoung Lee, Jin Seo Park, Seon-Eui Hong, Masao Taki, Kanako Wake, Joe Wiart, and Hyung-Do Choi. Brain sar of average male korean child to adult models for mobile phone exposure assessment. *Physics in Medicine & Biology*, 64(4):045004, 2019.

[MBC79] Michael D McKay, Richard J Beckman, and William J Conover. Comparison of three methods for selecting values of input variables in the analysis of output from a computer code. *Technometrics*, 21(2):239–245, 1979.

[MFE+17] Taghrid Mazloum, Bader Fetouri, Nabil Elia, Emmanuelle Conil, Christophe Grangeat, and Joe Wiart. Assessment of RF human exposure to LTE small-and macro-cells: UL case. In *2017 11th European Conference on Antennas and Propagation (EUCAP)*, pages 1592–1593. IEEE, 2017.

[MMDS03] DS Moore, GP McCabe, WM Duckworth, and SL Sclove. Bootstrap methods and permutation tests. *The Practice of Business Statistics: Using Data for Decisions, WH Freeman, New York*, 2003.

[PLL+06] A Pradier, F Lacroux, D Lautru, MF Wong, V Fouad Hanna, and J Wiart. SAR assessment using tissues Homogenization

Technique. In *2006 First European Conference on Antennas and Propagation*, pages 1–4. IEEE, 2006.

[RRS00] Sembiam R Rengarajan and Yahya Rahmat-Samii. The field equivalence principle: Illustration of the establishment of the non-intuitive null fields. *IEEE Antennas and Propagation Magazine*, 42(4):122–128, 2000.

[SK+63] Alan Stuart, Maurice G Kendall, et al. *The advanced theory of statistics*. Griffin, 1963.

[VBPG15] Roberto Vallauri, Giorgio Bertin, Bruno Piovano, and Paolo Gianola. Electromagnetic Field Zones Around an Antenna for Human Exposure Assessment: Evaluation of the human exposure to EMFs. *IEEE Antennas and Propagation Magazine*, 57(5):53–63, 2015.

[VKG12a] Blaž Valič, Bor Kos, and Peter Gajšek. Occupational exposure assessment on an FM mast: electric field and SAR values. *International journal of occupational safety and ergonomics*, 18(2):149–159, 2012.

[VKG12b] Blaž Valič, Bor Kos, and Peter Gajšek. Simultaneous occupational exposure to FM and UHF transmitters. *International journal of occupational safety and ergonomics*, 18(2):161–170, 2012.

[WHWB08] J Wiart, A Hadjem, MF Wong, and I Bloch. Analysis of RF exposure in the head tissues of children and adults. *Physics in Medicine & Biology*, 53(13):3681, 2008.

[Wia16] Joe Wiart. *Radio-frequency human exposure assessment: from deterministic to stochastic methods*. John Wiley & Sons, 2016.

[Yee66] Kane Yee. Numerical solution of initial boundary value problems involving maxwell's equations in isotropic media. *IEEE Transactions on antennas and propagation*, 14(3):302–307, 1966.

ECOLE
DOCTORALE

Titre : Evaluation de l'exposition en champ proche : nouvelle méthodologie et application aux fréquences FM pour l'exposition des travailleurs

Mots clés : Champ proche, Exposition, DAS, Pylônes FM, FDTD, Statistiques

Résumé : La radio FM reste populaire chez toutes les catégories du grand public. Les antennes FM sont généralement placées sur des structures métalliques, aussi appelées pylônes, que les travailleurs doivent escalader pour effectuer des travaux de maintenance. La législation exige le contrôle de l'exposition lorsque les travailleurs sont exposés à des émetteurs à haute puissance. L'objectif de cette recherche est de caractériser les champs électromagnétiques dans les environnements des pylônes et d'évaluer l'exposition.

Les champs électromagnétiques dans les environnements des pylônes sont généralement dans le champ proche des antennes, mais la caractérisation et la compréhension du champ proche dans la littérature est limitée à des cas spécifiques d'exposition. Cette recherche s'est donc focalisée sur la définition d'une nouvelle méthodologie en généralisant l'évaluation de l'exposition en champ proche.

Cette étude a examiné l'environnement des champs proches en analysant des indicateurs de champs électromagnétiques que l'on peut trouver dans les pylônes, pour ensuite générer des champs incidents aléatoires aux caractéristiques similaires. Les champs aléatoires ont été validés et sélectionnés par un procédé, pour ensuite effectuer des simulations FDTD pour évaluer le débit d'absorption spécifique (DAS).

Cinq cents simulations FDTD pour l'évaluation du DAS ont été effectuées. Les résultats montrent une forte corrélation entre le DAS local/corps entiers et le champ électrique moyen. Des modèles de substitution permettant de lier le DAS au champ électrique ont été trouvés en utilisant des techniques de Machine Learning. L'incertitude des résultats de DAS et des modèles de substitution a été quantifiée.

Title : Exposure Assessment in Near-field: New Methodology and Application in FM Frequencies for Occupational Exposure

Keywords : Near-field, Exposure, SAR, FM Pylons, FDTD, Statistics

Abstract : FM radio is still popular among all segments of the general population. FM antenna arrays are usually placed on metallic structures known as pylons that workers have to climb in order to do maintenance and repair work. Exposure monitoring is required by regulation when workers are exposed to high-power emitters. The purpose of this research is to characterize electromagnetic fields (EMF) in pylon environments and to assess EMF exposure in such cases.

EMF in pylon environments tend to be in the near-field region of the antenna arrays, but the characterization and understanding of such environments in the literature is limited to specific exposure cases. This research has therefore focused on defining a new methodology by generalizing exposure assessment in the near-field.

Using field metrics analysis in human-sized volumes, this study analyzed the near-field environments found in the transmission pylons and generated random incident fields that have the same characteristics. The random incident fields were subjected to a validation and selection process in order to be used in FDTD simulations for specific absorption rate (SAR) assessment.

Five hundred FDTD simulations for SAR assessments were performed. The results showed a high correlation between local & whole-body SAR and averaged electric field strength. Surrogate models linking SAR to electric field strength were built using machine learning techniques. The uncertainty of the SAR results and the surrogate models was quantified.

Institut Polytechnique de Paris
91120 Palaiseau, France